Article

Cell Reports

Targeting senescent cells improves functional recovery after spinal cord injury

Graphical abstract

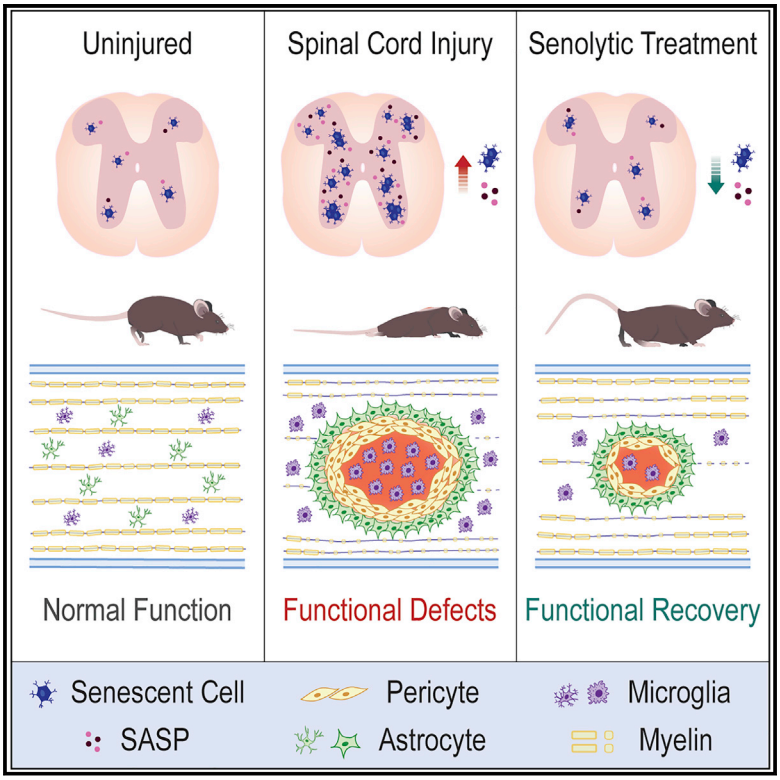

Authors

Diogo Paramos-de-Carvalho, Isaura Martins, Ana Margarida Cristóvão, ..., Ana Farinho, António Jacinto, Leonor Saúde

Correspondence

msaude@medicina.ulisboa.pt

In brief

Paramos-de-Carvalho et al. demonstrate that cellular senescence is induced in the spinal cord upon injury. Targeting senescent cells with senolytic drugs improves functional recovery after injury by promoting myelin sparing, reducing the fibrotic scar, and attenuating inflammation, which are correlated with decreased levels of pro-fibrotic and pro-inflammatory factors in the microenvironment.

Highlights

- Senescent cells are induced at the lesion periphery upon spinal cord injury
- Administration of senolytic drugs promotes locomotor and sensory recovery
- ABT-263 treatment suppresses pro-inflammatory and pro-fibrotic SASP responses
- Targeting senescent cells favors a pro-repair microenvironment after injury

Paramos-de-Carvalho et al., 2021, Cell Reports *36*, 109334
July 6, 2021
https://doi.org/10.1016/j.celrep.2021.109334

CellPress

Cell Reports

CellPress
OPEN ACCESS

Article

Targeting senescent cells improves functional recovery after spinal cord injury

Diogo Paramos-de-Carvalho,[2,3,4] Isaura Martins,[2,4] Ana Margarida Cristóvão,[2] Ana Filipa Dias,[2] Dalila Neves-Silva,[2] Telmo Pereira,[3] Diana Chapela,[2] Ana Farinho,[3] António Jacinto,[3] and Leonor Saúde[1,5,*]

[1]Instituto de Medicina Molecular – João Lobo Antunes e Instituto de Histologia e Biologia do Desenvolvimento, Faculdade de Medicina da Universidade de Lisboa, 1649-028 Lisboa, Portugal

[2]Instituto de Medicina Molecular – João Lobo Antunes, Faculdade de Medicina da Universidade de Lisboa, 1649-028 Lisboa, Portugal

[3]CEDOC, NOVA Medical School, Faculdade de Ciências Médicas da Universidade Nova de Lisboa, 1150-082 Lisboa, Portugal

[4]These authors contributed equally

[5]Lead contact

*Correspondence: msaude@medicina.ulisboa.pt

https://doi.org/10.1016/j.celrep.2021.109334

SUMMARY

Persistent senescent cells (SCs) are known to underlie aging-related chronic disorders, but it is now recognized that SCs may be at the center of tissue remodeling events, namely during development or organ repair. In this study, we show that two distinct senescence profiles are induced in the context of a spinal cord injury between the regenerative zebrafish and the scarring mouse. Whereas induced SCs in zebrafish are progressively cleared out, they accumulate over time in mice. Depletion of SCs in spinal-cord-injured mice, with different senolytic drugs, improves locomotor, sensory, and bladder functions. This functional recovery is associated with improved myelin sparing, reduced fibrotic scar, and attenuated inflammation, which correlate with a decreased secretion of pro-fibrotic and pro-inflammatory factors. Targeting SCs is a promising therapeutic strategy not only for spinal cord injuries but potentially for other organs that lack regenerative competence.

INTRODUCTION

A spinal cord injury is a major cause of disability in humans and other mammals, often leading to permanent loss of locomotor and sensory functions. This type of traumatic lesion is defined by three biological features: a lesion core or fibrotic scar with no viable neural tissue; an astrocytic scar around the lesion core; and a surrounding area of spared neural tissue with limited function, which may exhibit some functional plasticity (O'Shea et al., 2017). Although the lesion scar provides structural support, it also creates an inhibitory microenvironment for the regrowth of severed axons, thus preventing re-enervation of the original targets (Cregg et al., 2014). A spinal cord injury is further defined as an inflammatory condition mediated by activated astrocytes and infiltrating macrophages that remain in the spinal cord indefinitely (Donnelly and Popovich, 2008). Immediately after the injury, the blood-spinal cord barrier is disrupted and, although it gradually recovers, it remains compromised for a long period of time (Whetstone et al., 2003). This facilitates the extravasation of immune cells contributing to the establishment of a chronic inflammatory state (Beck et al., 2010).

In contrast to mammals, the zebrafish spinal cord has the remarkable capacity to recover motor and sensory functions after injury. This regenerative ability seems to stem from the supportive microenvironment where there is no formation of a glial or fibrotic scar and inflammation is dynamically controlled by macrophages (Tsarouchas et al., 2018), allowing neurogenesis and regrowth of severed axons (Becker et al., 1997; Vajn et al., 2013).

While considerable knowledge was achieved on the biological processes that occur after a spinal cord injury in mammals and regenerative species, small progress was obtained on therapeutic options, suggesting that other cellular players might be relevant following an injury. Senescence is a cellular concept traditionally seen as a permanent cell-cycle arrest response related to aging (van Deursen, 2014; Gorgoulis et al., 2019; Herranz and Gil, 2018). Studies in recent years changed the way we perceive cellular senescence, placing it at the center of tissue remodeling in disease settings by limiting fibrosis, namely in wound healing (Demaria et al., 2014; Jun and Lau, 2010), damaged livers (Kong et al., 2012; Krizhanovsky et al., 2008), and infarcted hearts (Meyer et al., 2016). In models with high regenerative abilities, such as salamander limbs, zebrafish hearts and fins, and neonatal mouse hearts, a burst of transient senescent cells (SCs) was shown to be induced after an injury (Sarig et al., 2019; Da Silva-Álvarez et al., 2019; Yun et al., 2015). These cells were shown to be efficiently cleared from the tissues as regeneration progressed, possibly by macrophages (Yun et al., 2015). Remarkably, if this initial senescence is depleted, zebrafish fin

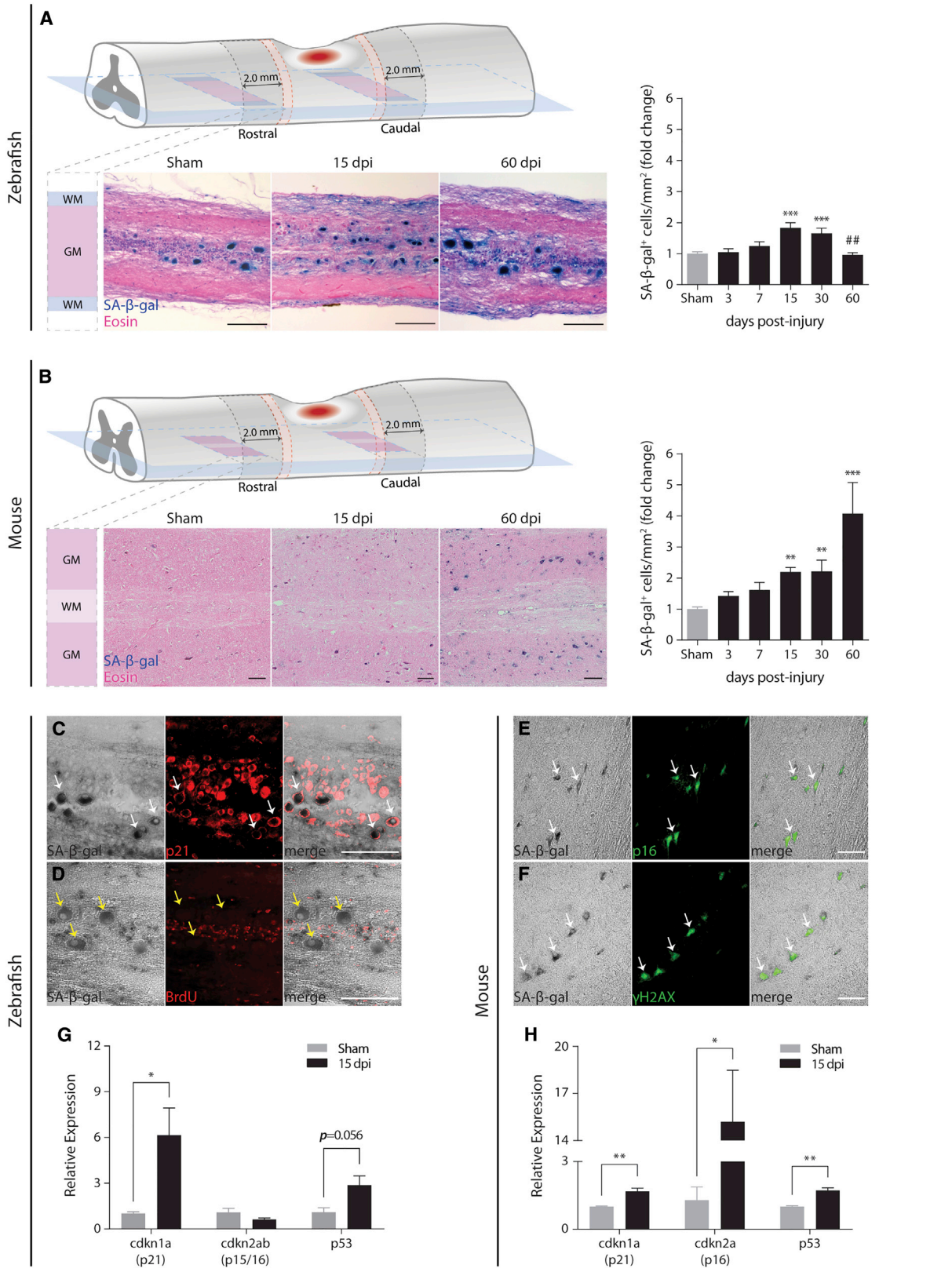

(legend on next page)

regeneration is impaired (Da Silva-Álvarez et al., 2019), suggesting that a transient accumulation of SCs appears to have beneficial functions. Alternatively, persistent senescence is detrimental for tissue and organ function in aging and aged-related diseases, such as atherosclerosis, osteoporosis, diabetes, and neurodegeneration (Calcinotto et al., 2019). Key to their various roles is the fact that SCs secrete a plethora of factors known as senescence-associated secretory phenotype (SASP) (Krtolica et al., 2001). It is through their SASP that SCs communicate with neighboring cells and modulate the tissue microenvironment, thus exerting most of their physiological effects (Acosta et al., 2013; Calcinotto et al., 2019). Importantly, the SASP mediates paracrine senescence, a process where SCs induce neighboring cells to undergo senescence (Acosta et al., 2013). It is becoming accepted that the beneficial versus detrimental effects of the SASP depend not only on its composition and stage of senescence progression, but also on the cell type affected and the stressor/injury type (Herranz and Gil, 2018).

Considering that persistent senescence was shown to be harmful, we hypothesized that accumulation of SCs contributes to the failure of spinal cord regeneration observed in mammals. In agreement with this hypothesis, we have shown that SCs are induced after spinal cord injury in both zebrafish and mice. While induced SCs in the zebrafish spinal cord progressively decrease, in mice these cells increase over time. We demonstrate that pharmacological depletion of SCs during the subacute post-injury phase in mice seems to attenuate the secondary damage and maximize the extent of spared tissue by decreasing inflammation burden, scar extension, and demyelination, leading to a better functional outcome. Therefore, our data support the potential use of therapeutics targeting SCs to promote neuroprotection in the context of spinal cord injuries.

RESULTS

Zebrafish and mice exhibit distinct senescence profiles after spinal cord injury

A transient senescent profile was recently described in several regenerating organs after an injury (Sarig et al., 2019; Da Silva-Álvarez et al., 2019; Yun et al., 2015), but the senescence profile in injured non-regenerating organs has been poorly characterized.

To determine whether senescence is induced following a spinal cord lesion in zebrafish and in mice, we used the gold standard method to identify SCs, that is, the senescence-associated β-galactosidase (SA-β-gal) assay (Itahana et al., 2007). In zebrafish, an animal with high regenerative abilities, SA-β-gal$^+$ cells were found mainly in the gray matter of the spinal cord ventral horn of sham-injured animals (Figure 1A). Upon an injury, these cells were induced at the lesion periphery, reaching a peak at 15 days post-injury (dpi), when they double in number, and then returning to basal levels at 60 dpi (Figure 1A). In mice, an animal with limited regenerative capacity, SA-β-gal$^+$ cells were also detected mainly in the gray matter of the spinal cord ventral horn of sham-injured animals and induced at the lesion periphery upon injury (Figure 1B). However, in clear contrast to the zebrafish, these SA-β-gal$^+$ cells did not return to basal levels and instead accumulated over time, reaching a 4-fold increase at 60 dpi, when compared with sham animals (compare Figures 1A and 1B). Importantly, we confirmed that these profiles were injury-driven and not age-dependent by showing that the number of SA-β-gal$^+$ cells remained unchanged in the spinal cord of sham-injured animals of different ages, spanning all experimental time points of this study (Figures S1A and S1B). The existence of cell and matrix debris at the lesion core did not allow reliable quantifications of SA-β-gal$^+$ cells in this region. Yet, we cannot discard the possible existence and/or induction of SCs in the injury core. We further confirmed by immunofluorescence the association of SA-β-gal$^+$ cells with several senescence-associated biomarkers (Calcinotto et al., 2019). In zebrafish, we were able to show that, at 15 dpi, SA-β-gal$^+$ cells co-localized with the cell cycle arrest marker p21^{CIP1} (Figure 1C) and were devoid of the proliferation marker 5-bromo-2′-deoxyuridine (BrdU) (Figure 1D). In mice, SA-β-gal$^+$ cells co-localized with the cell cycle arrest marker p16^{INK4a} (Figure 1E) and the DNA damage marker γH2AX (Figure 1F). In zebrafish and in mice, some SA-β-gal$^+$ cells exhibited a clear enlarged morphology, another hallmark of SCs (Narita et al., 2003). In sham-injured animals, SA-β-gal$^+$ cells also displayed immunoreactivity for p21^{CIP1} (zebrafish) and p16^{INK4a} (mice) (Figures S1C and S1D). However, the expression of these senescence biomarkers was

Figure 1. Different senescent cell dynamics are induced after spinal cord injury in zebrafish and in mice

(A and B) SA-β-gal$^+$ cells (blue) were detected and quantified in non-injured (sham) and injured zebrafish spinal cords at different time points (3, 7, 15, 30, and 60 days post-injury [dpi]). n = 5–16. Similarly, SA-β-gal$^+$ cells were detected and quantified in mouse laminectomized (sham) and injured spinal cords at the same time points. n = 4–16. Eosin counterstaining was performed after cryosectioning. Cells were quantified at the lesion periphery along 2.0 mm in longitudinal sections spanning the ventral horn. A 0.5-mm interval (red dashed zone) was established between the lesion border and the beginning of the quantification region. SA-β-gal$^+$ cells were only quantified in the gray matter (GM) and not in the white matter (WM). Quantifications are presented as fold change toward sham. In zebrafish, SA-β-gal$^+$ cells reach a peak at 15 dpi (238.6 cells/mm^2), a 2-fold increase compared to sham (127.2 cells/mm^2). In mice, SA-β-gal$^+$ cells display a 4-fold increase at 60 dpi (80.0 cells/mm^2) toward sham (19.0 cells/mm^2). Data are presented as mean ± SEM. *p < 0.05, **p < 0.01, ***p < 0.001, versus sham; $^{\#\#}$p < 0.01, 60 versus 30 dpi. Scale bars, 100 μm.

(C and D) In zebrafish, SA-β-gal$^+$ cells co-localized with the senescence biomarker p21 and were devoid of the proliferation marker BrdU. Images were taken at 15 dpi. White arrows point to representative examples of co-localization, while yellow arrows point to the absence of co-localization. Scale bars, 100 μm.

(E and F) In mice, a similar co-localization was found between SA-β-gal$^+$ cells and the senescence biomarkers p16 and γH2AX. White arrows point to representative examples of co-localization. Scale bars, 100 μm.

(G and H) At 15 dpi, the expression of senescence biomarkers, namely *cdkn1a* (encodes for p21), *cdkn2ab* (encodes for p15/16 in zebrafish), *cdkn2a* (encodes for p16 in mice), and *p53*, was evaluated by qPCR. Results are presented as relative expression toward sham. Data are presented as mean ± SEM. *p < 0.05, **p < 0.01, versus sham.

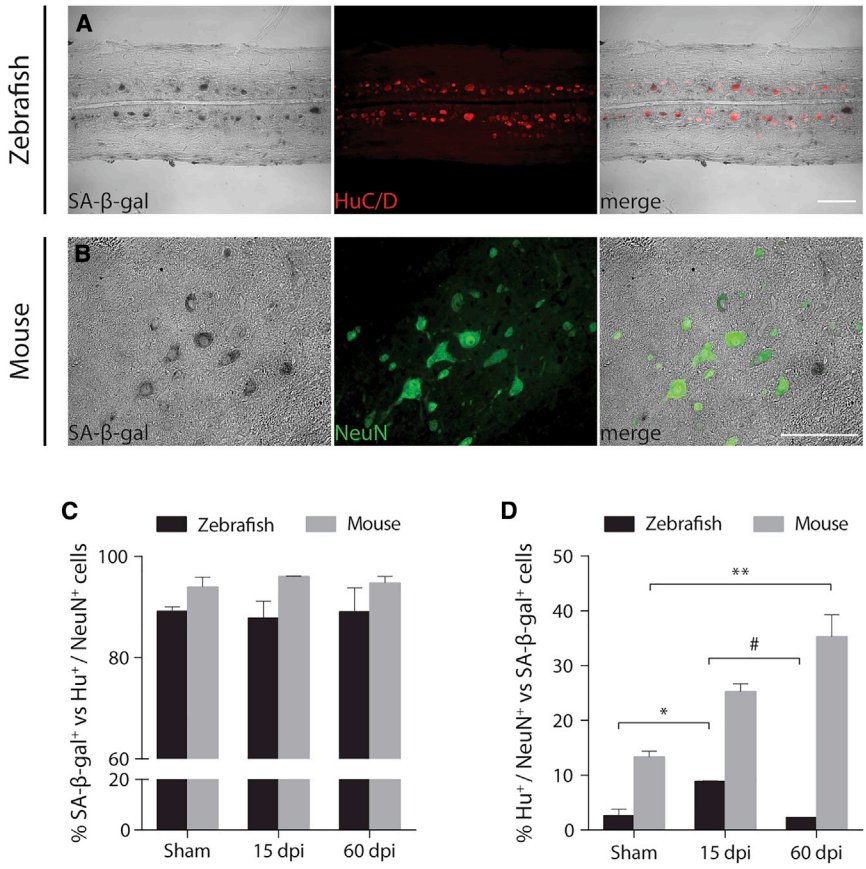

Figure 2. Different profiles of SA-β-gal$^+$ neuronal populations between zebrafish and mouse

(A and B) In zebrafish and mice, SA-β-gal$^+$ cells (black) co-localized with the neuronal markers (A) HuC/D (red) and (B) NeuN (green), respectively. Representative images were taken at 15 days post-injury (dpi). Scale bars, 100 μm.

(C and D) Percentages of total SA-β-gal$^+$ cells that are HuC/D$^+$ or NeuN$^+$ and of total HuC/D$^+$ or NeuN$^+$ neurons that are SA-β-gal$^+$ are compared between both models. Cells were quantified at the lesion periphery along 2.0 mm in longitudinal sections. A 0.5-mm interval was established between the lesion border and the beginning of the quantification region. Quantifications are presented for uninjured/laminectomized (sham) zebrafish/mice at 15 and 60 dpi. n = 2–4. Data are presented as mean ± SEM. *p < 0.05, **p < 0.01, versus sham; #p < 0.05, versus 15 dpi.

significantly increased upon injury (Figures 1G and 1H). In zebrafish spinal cords, we observed an augmented expression of *cdkn1a* (which encodes for p21) and *p53*, another important cell cycle regulator (Figure 1G). No differences were found in the expression of *cdkn2ab* (encodes for p15/p16 in zebrafish). In mouse spinal cords, we detected an increased expression of *cdkn1a*, *cdkn2a* (encodes for p16), and *p53* (Figure 1H). Altogether, these results reveal two clearly distinct senescence profiles in an injured spinal cord, a transient profile observed in regenerative zebrafish and a persistent one observed in scarring mice.

SCs in the zebrafish and mouse spinal cord are mostly neurons

To identify which cell types comprise the senescent SA-β-gal$^+$ population, we searched for co-localization with cell type-specific markers using seriated slides from the same samples of the initial characterization. We observed that most SA-β-gal$^+$ cells detected in the gray matter at the lesion periphery co-localized with known neuronal markers, namely HuC/D (Figure 2A) and NeuN (Figure 2B). In injured zebrafish spinal cords, 87.8%–89.1% of SA-β-gal$^+$ cells detected in the gray matter co-localized with HuC/D at 15 and 60 dpi, respectively (Figure 2C). Similarly, in mouse spinal cords, 94.8%–96.0% of SA-β-gal$^+$ cells detected in the gray matter co-localized with the pan-neuronal marker NeuN at 15 and 60 dpi, respectively. When we calculated the percentage of SA-β-gal$^+$ cells of the total neuronal population at the lesion periphery, we again observed two distinct profiles between these two models. In zebrafish, the percentage of total neurons that are SA-β-gal$^+$ reaches a peak of 8.9% at 15 dpi and then returns to basal levels (2.3%) at 60 dpi. Alternatively, mice display 25.3% of senescent neurons at 15 dpi (Figure 2D), and this number keeps increasing until 60 dpi, reaching 35.3% of total neurons.

Targeting SCs with senolytic drugs improves motor, sensory, and bladder functions in a mouse spinal cord contusion injury model

The role of senescence in diverse biological contexts is still poorly understood. Yet, it is accepted that accumulation or persistence of SCs and subsequent chronic exposure to their SASP contribute to loss of tissue function and diminish the repair capacity in aged tissues (Acosta et al., 2013; Calcinotto et al., 2019; Campisi, 2013; Childs et al., 2015).

We hypothesized that accumulation of SCs in the mouse spinal cord is an important factor for the inhibitory microenvironment that undermines the regenerative potential after an injury. To evaluate the impact of depleting SCs in a mouse contusion model of spinal cord injury, we used the ABT-263 drug, known to work as a powerful senolytic (Zhu et al., 2016). We administered ABT-263 within the first 14 dpi (subacute injury phase), during which the blood-spinal cord barrier remains leaky (Whetstone et al., 2003), thus ensuring maximum accessibility of this drug to the tissue (Figure 3A).

Before injury, all mice presented a normal locomotor behavior in the open field test, which corresponds to the maximum score of 9 in the Basso Mouse Scale (BMS) (Basso et al., 2006). After injury, most injured mice exhibited complete hindlimb paralysis

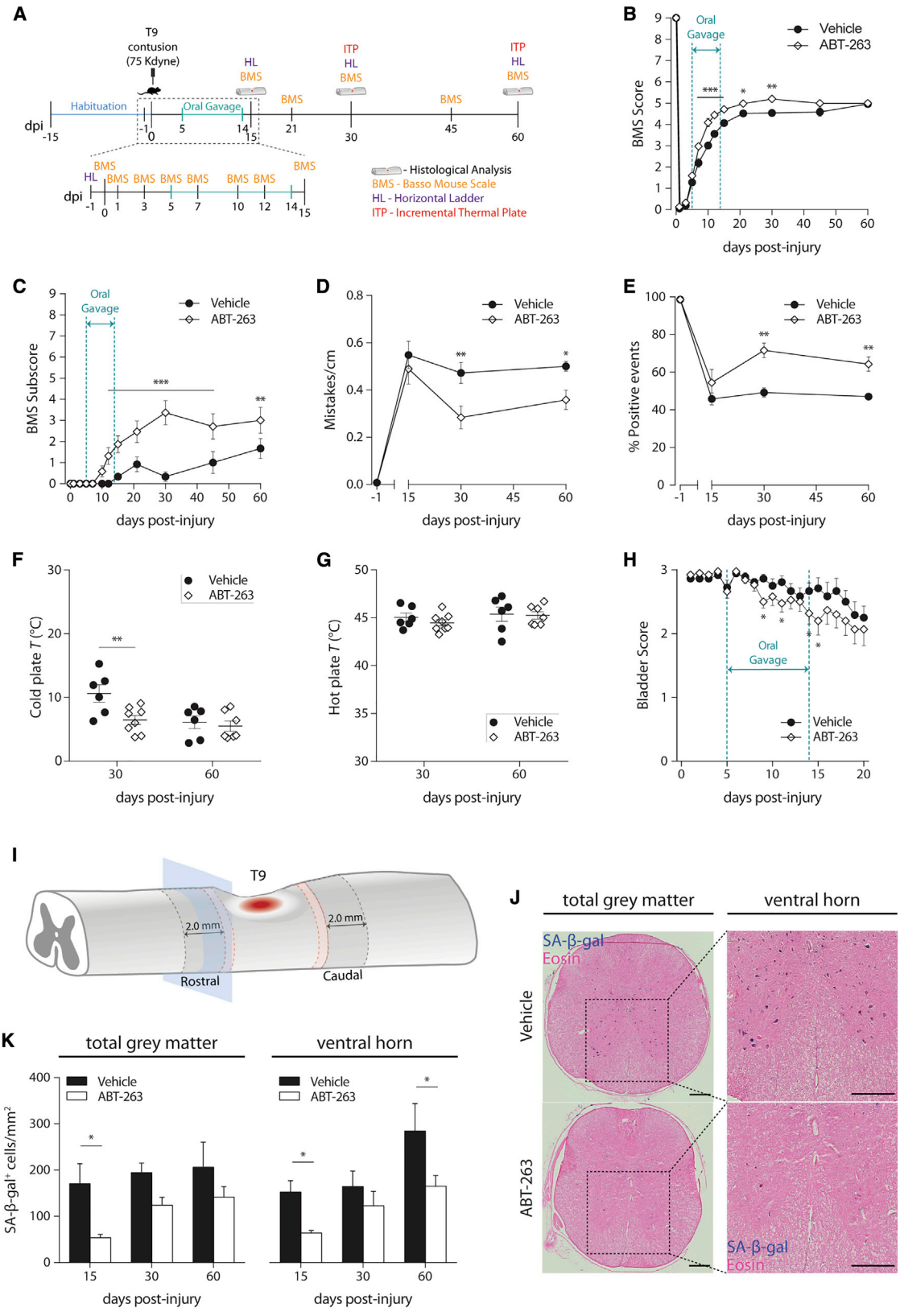

(legend on next page)

at 1 dpi and gradually improved locomotor ability reaching a plateau at around 21 dpi (Figure 3B), similarly to what has been previously described for a contusion injury model in C57BL/6J mice (Basso et al., 2006). In ABT-263-treated animals, BMS scores were significantly higher from 7 until 30 dpi (Figure 3B) and BMS subscores were significantly higher from 12 to 60 dpi (Figure 3C), when compared with animals treated with vehicle. At 30 dpi, all ABT-263-treated mice achieved frequent plantar stepping with 93% (14 out of 15) of mice displaying parallel placement of both hindpaws at initial contact and 40% (6 out of 15) also at lift off. Remarkably, 33% (5 out of 15) of mice treated with ABT-263 exhibited consistent plantar stepping and mild trunk stability, one animal showed normal trunk stability with mostly coordinated forelimb-hindlimb walking, and a second animal displayed some forelimb-hindlimb coordination, improvements never achieved in vehicle-treated mice.

A finer assessment of locomotion was performed using the horizontal ladder (HL) test. Prior to the injury, all mice completed the HL test with few to no mistakes or negative events (Figures 3D and 3E). Animals treated with ABT-263 made significantly fewer stepping mistakes (Figure 3D) and displayed significantly more positive stepping events (Figure 3E) at 30 and 60 dpi, when compared with vehicle-treated mice, thus largely corroborating the results obtained in the open field.

Thermal allodynia, i.e., hypersensitivity to normally non-noxious stimuli, is a common pain-related symptom associated with spinal cord injuries (Nakae et al., 2011; Watson et al., 2014). Using an incremental thermal plate (ITP), we could compare the temperature threshold necessary to elicit an avoidance behavior to a cold or hot stimulus between the two experimental groups. Considering that uninjured C57BL/6J mice only exhibit a nocifensive reaction to cold between 2°C and 4°C (Yalcin et al., 2009), ABT-263 treatment significantly decreased cold hypersensitivity at 30 dpi (6.4°C), compared to vehicle-treated animals who showed an average temperature reaction to cold of 10.6°C (Figure 3F). We found no effect of ABT-263 administration on the threshold temperature required to prompt a nocifensive reaction to a hot stimulus when compared to vehicle administration (Figure 3G).

Another common consequence of spinal cord injury is bladder dysfunction (Yoshimura, 1999). We assessed bladder function by attributing a score to the amount of urine retained each day. In contrast to injured mice treated with vehicle, injured mice treated with ABT-263 exhibited smaller volumes of retained urine from 9 to 20 dpi (Figure 3H), an effect that was lost after 20 dpi (data not shown).

We demonstrate that ABT-263 administration by oral gavage from 5 to 14 dpi reduced the number of SA-β-gal$^+$ cells in the spinal cord at the lesion periphery, when compared to vehicle administration (Figures 3I–3K). SA-β-gal$^+$ cells were quantified along transversal spinal cord sections spanning the lesion periphery (Figure 3I). We performed two separate quantifications—one covering the total gray matter area and other only in the ventral horn—in order to assess the effect of ABT-263 along the whole dorsal-ventral axis but also to have a more direct comparison with the initial characterization profile (Figure 3J). Targeting SCs during the subacute phase of the injury significantly decreased the number of SA-β-gal$^+$ cells by 68.4% (total gray matter) and 58% (ventral horn), preventing their accumulation at 15 dpi (Figure 3K). Although SA-β-gal$^+$ cells seemingly start to re-emerge following the end of the senolytic administration period, these were still significantly reduced in the ventral horn region at 60 dpi (Figure 3K). We also show that ABT-263 treatment leads to a reduction in the levels of p16 protein and *cdkn2a* expression (Figures S2A and S2B). In addition, there was a decreased immunoreactivity for γH2AX in ABT-263-treated spinal cords (Figure S2C). These results thus confirm the senolytic activity of ABT-263 in the mouse spinal cord.

In a completely independent study, we targeted SCs with a cocktail of two different drugs, dasatinib plus quercetin (D+Q), known to have a strong senolytic activity (Zhu et al., 2015), using the same injury parameters and administration time window for the sake of comparison (Figures S3A–S3C). D+Q-treated animals exhibited a significantly improved locomotor function after a spinal cord injury toward vehicle-treated mice, resulting in higher BMS scores (Figures S3D and S3E) and improved HL performances (Figures S3F and S3G). Similarly to ABT-263, D+Q administration also decreased the hypersensitivity to a cold stimulus at 30 dpi (Figure S3H), while no effects were observed in response to a hot stimulus (Figure S3I). These results corroborate those obtained with ABT-263, reinforcing the positive

Figure 3. Targeting senescent cells with ABT-263 improves motor, sensory, and bladder function recovery following a spinal cord injury in mice

(A) Schematic of the experimental setup. Animals were habituated to the different behavioral setups for a 15-day period, before being submitted to a moderate-to-severe (force, 75 Kdyne; displacement, 550–750 μm) T9 contusion injury. Injured animals received daily vehicle or ABT-263 via oral gavage, from 5 to 14 dpi.
(B and C) Basso Mouse Scale (BMS) score and subscore were evaluated in an open field at different time-points (0, 1, 3, 5, 7, 10, 12, 15, 21, 30, 45, and 60 dpi). n = 18–19.
(D and E) The locomotor performance in the horizontal ladder (HL) was assessed at −1 (control), 15, 30, and 60 dpi by quantifying the total number of mistakes per centimeter and the percentage of singular positive events (plantar step, toe step, and skip) measured and averaged across three successful trials. n = 3-6.
(F and G) Thermal allodynia was tested at 30 and 60 dpi by determining the temperature at which injured mice reacted to a cold or hot stimulus. n = 6–8.
(H) Bladder function was grossly evaluated by attributing a bladder score to the amount of urine collected each time a bladder was manually voided. n = 18–19.
(I) SA-β-gal$^+$ cells were quantified in a total of 10 different transversal sections (5 rostral and 5 caudal) along 2.0 mm at the lesion periphery. A 0.5-mm interval (red dashed zone) was established between the lesion and the beginning of the quantification region.
(J) Eosin counterstaining was performed after cryosectioning. SA-β-gal$^+$ cells (blue) were quantified in the total sectional gray matter and only at the ventral horn. Scale bars, 200 μm.
(K) Quantifications were performed at all experimental endpoints (15, 30, and 60 dpi). At 15 dpi, ABT-263 treatment significantly decreased the number of SA-β-gal$^+$ cells/mm^2 in the total gray matter and in the ventral horn by 68.4% and 58.0%, respectively. At 60 dpi, a significant reduction (41.9%) of SA-β-gal$^+$ cells/mm^2 in ABT-263-treated animals was still observed in the ventral horn.
n (15 dpi) = 3–4; n (30 dpi) = 3–4; n (60 dpi) = 2–3. Data are presented as mean ± SEM. *p < 0.05, **p < 0.01, ***p < 0.001, ABT-263 versus vehicle.

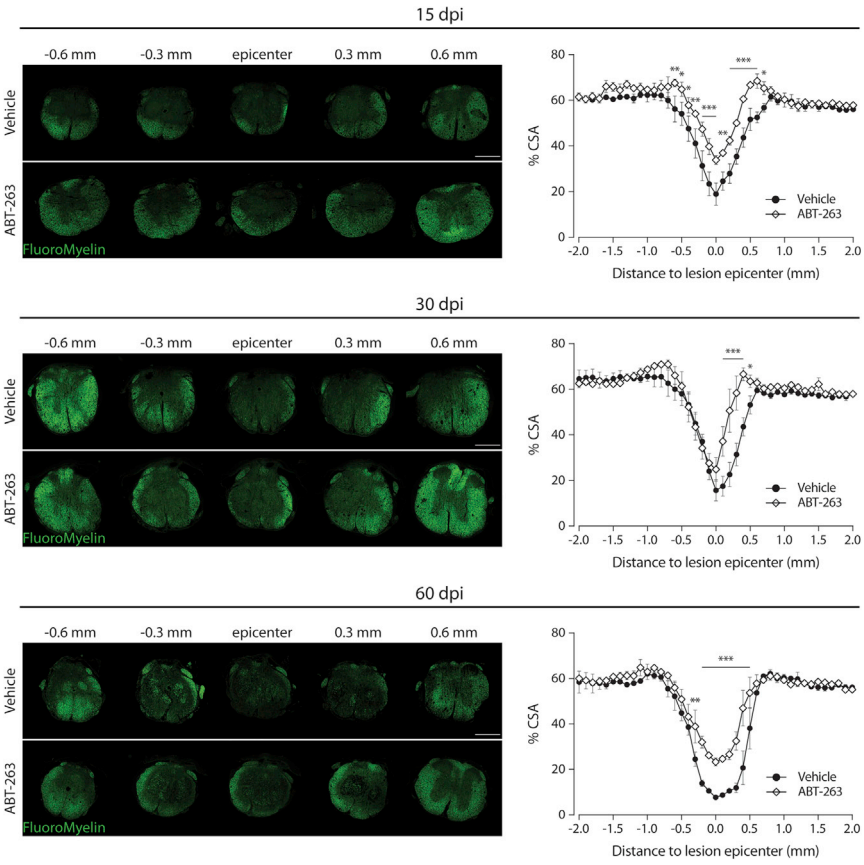

Figure 4. White matter sparing is increased after targeting senescent cells with ABT-263

Transversal sections at different distances from the lesion epicenter of an injured spinal cord at 15, 30 and 60 dpi, treated with vehicle or ABT-263, and stained with FluoroMyelin (green) and the corresponding quantifications. White matter sparing was assessed by normalizing the area stained with FluoroMyelin (green) to the total cross-sectional area (CSA) of spinal cord sections every 100 μm ranging from 2 mm rostral and 2 mm caudal to the lesion epicenter. Scale bars, 500 μm. n (15 dpi) = 3–4; n (30 dpi) = 3–4; n (60 dpi) = 2–3. Data are expressed as % CSA and presented as mean ± SEM. *p < 0.05, **p < 0.01, ***p < 0.001, ABT-263 versus vehicle.

effect of targeting SCs on locomotor and sensory recovery after a spinal cord injury in mammals. In accordance, the D+Q cocktail significantly decreased the number of SA-β-gal$^+$ cells at the lesion periphery (Figure S3J), thus confirming its senolytic effect in the mouse spinal cord.

The senolytic ABT-263 promotes myelin preservation after spinal cord injury

After a spinal cord injury, oligodendrocytes undergo both necrotic and apoptotic cell death, which results in demyelination around the lesion, impairing function of unprotected fibers, contributing to the accumulation of cell debris, and potentiating the inhibitory microenvironment for repair (Crowe et al., 1997; Emery et al., 1998; Totoiu and Keirstead, 2005). To evaluate the effect of depleting SCs on the demyelination status after injury, we used FluoroMyelin green fluorescent myelin staining to compare the spared white matter area per total cross-sectional area (% CSA) between ABT-263-treated mice and vehicle-treated mice along 2 mm around the lesion epicenter. Treatment with ABT-263 consistently resulted in significantly greater white matter sparing levels across all experimental time points, an effect that at 30 dpi was more prominent at the caudal side of the lesion (Figure 4).

The normal neuronal circuit organization is disrupted after a spinal cord injury. However, spared neural tissue can, to a certain extent (depending on the severity of the lesion), reorganize itself in order to establish new lines of communication across and beyond the injury (Courtine and Sofroniew, 2019). This plasticity potential explains why after an incomplete lesion (e.g., our contusion injury model) mice can partially restore their locomotor function.

Considering that ABT-263 increased the amount of spared myelin, we hypothesized that targeting SCs would also provide a more favorable environment for axonal preservation and growth after a spinal cord injury. To assess this, we tested the expression of neuronal growth-associated protein 43 (GAP43), which is highly expressed in neuronal growth cones during development and axonal regeneration (Benowitz and Routtenberg, 1987). Although GAP43 staining does not allow us to discriminate between new axons and spared ones, it is an intrinsic determinant of neuronal plasticity and strongly correlates with enhanced regenerative capacity (Mason et al., 2002). We performed immunostainings for GAP43 in dorsal-ventral longitudinal sections spanning the ventral horn (where the motor neurons are located) and quantified the number of GAP43$^+$ fibers at specific distances from the lesion epicenter (Figures S4A and S4B), as previously described (Almutiri et al., 2018; Hata et al., 2006). At 30 and 60 dpi, ABT-263-treated mice had a significantly increased number of GAP43$^+$ axons at the caudal side of the lesion, compared to vehicle-treated mice (Figure S4B and S4C).

Administration of the senolytic ABT-263 reduces the fibrotic scar

Scar formation following spinal cord injury constitutes a major barrier for axonal regrowth (Cregg et al., 2014). Inside the lesion core, a subset of proliferating PDGFRβ$^+$ perivascular cells give rise to a fibrotic scar with dense deposition of extracellular matrix components (Soderblom et al., 2013). In fact, it has been shown that reducing the pericyte-derived fibrotic scar facilitates functional recovery after spinal cord injury in mice (Dias et al., 2018). We examined the size and length of the fibrotic scar using

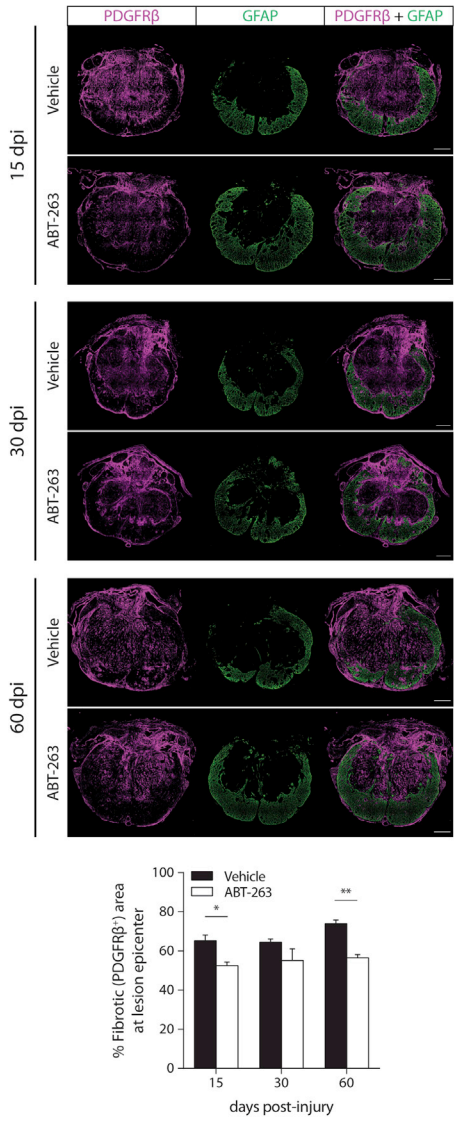

Figure 5. Targeting senescent cells leads to a reduction of the fibrotic scar

Transversal sections at the lesion epicenter of an injured spinal cord at 15, 30, and 60 dpi treated with vehicle or ABT-263 and stained with the fibrotic scar marker PDGFRβ$^+$ (magenta) and with the astrocytic scar marker GFAP (green). The fibrotic scar area was evaluated by normalizing the PDGFRβ$^+$ area to the total cross-sectional area at the lesion epicenter. GFAP$^+$ tissue surrounds the fibrotic core. Scale bars, 200 μm. n (15 dpi) = 3–4; n (30 dpi) = 3–4; n (60 dpi) = 2–3. The lower panel shows the percentage of fibrotic tissue in the injury core as quantified at 15, 30 and 60 dpi. Data are presented as mean ± SEM. *p < 0.05, **p < 0.01, ABT-263 versus vehicle.

a double immunostaining with PDGFRβ (a pericyte marker that labels the fibrotic component of the scar) and GFAP (a glial marker that helps delineate the fibrotic scar compartment). At the lesion epicenter, mice treated with the senolytic exhibited a significantly reduced PDGFRβ$^+$ area at 15 and 60 dpi when compared to mice treated with vehicle (Figure 5). Using the same double immunostaining, we were able to define the extension of the scar by tracing, rostrally and caudally to the epicenter, signs of fibrotic PDGFRβ$^+$ staining in the dorsal side of the spinal cord (Figure S5A). With this analysis, we observed that the total length of the fibrotic scar was shorter at 15 dpi in ABT-263-treated mice, an effect sustained until 30 dpi only at the caudal side (Figure S5B).

Macrophage numbers at the injury site are reduced following ABT-263 treatment

A spinal cord lesion in mice elicits a strong and long-lasting inflammatory response that potentiates secondary injury (Blight, 1985; Popovich et al., 1997). Macrophages are the most abundant inflammatory cells in a spinal lesion, infiltrating the injury core and releasing several molecules, namely nitrogen/oxygen metabolites, cytokines, proteases, and chondroitin sulfate proteoglycans that can cause cellular damage and inhibit axonal growth (Fitch and Silver, 1997). Importantly, depletion of macrophages was demonstrated to promote repair and partial motor recovery after spinal cord injury in rats (Popovich et al., 1999). Additionally, senescence is closely linked to inflammation. SCs, through their SASP, can secrete a plethora of immune modulators and proinflammatory cytokines such as tumor necrosis factor (TNF)-α, macrophage colony-stimulating factor (M-CSF), and CCL2 (three potent macrophage recruiters), as well as interleukin (IL)-6, IL-8, and IL-1α (Coppé et al., 2010). Therefore, the accumulation/persistence of SCs in tissues is usually associated with chronic inflammation. To investigate the impact of the accumulation of SCs on inflammation in the mouse spinal cord after an injury, we performed immunostainings with the pan-macrophage marker F4/80. As anticipated, by depleting SCs with ABT-263, we observed lower levels of inflammatory macrophages (% F4/80$^+$ area) in spinal cord sections spanning the lesion area, particularly at 15 and 30 dpi (Figure 6).

Targeting SCs downregulates key pro-fibrotic and pro-inflammatory secreted factors induced upon spinal cord injury

SCs modulate the surrounding tissue microenvironment and exert their pathophysiological effects through their SASP (Coppé et al., 2010; Acosta et al., 2013). Therefore, the timely clearance of SCs, in a given setting, seems to be critical to prevent chronic and uncontrolled SASP responses.

We conducted a separate study to evaluate the abundance of secreted factors in the injured spinal microenvironment at 15 dpi using a cytokine array. In this second study, the injury biomechanics and behavioral locomotor scores were similar and comparable to those previously observed (Figure S6). Also, in this study sham-injured animals were included to assess the response of every factor in the context of our spinal cord injury model. Thus, the amount of each factor was compared between sham, vehicle-treated, and ABT-263-treated mice (Figure S7). From a total of 111 factors present in the array, 26 were both upregulated upon injury (sham versus vehicle) and significantly decreased after ABT-263 treatment (vehicle versus ABT-263) (Figure 7). Factors were grouped according to their known roles, although some of them are not exclusive of their attributed group and may have additional roles. Some of the identified factors, such as amphiregulin, platelet-derived growth factor

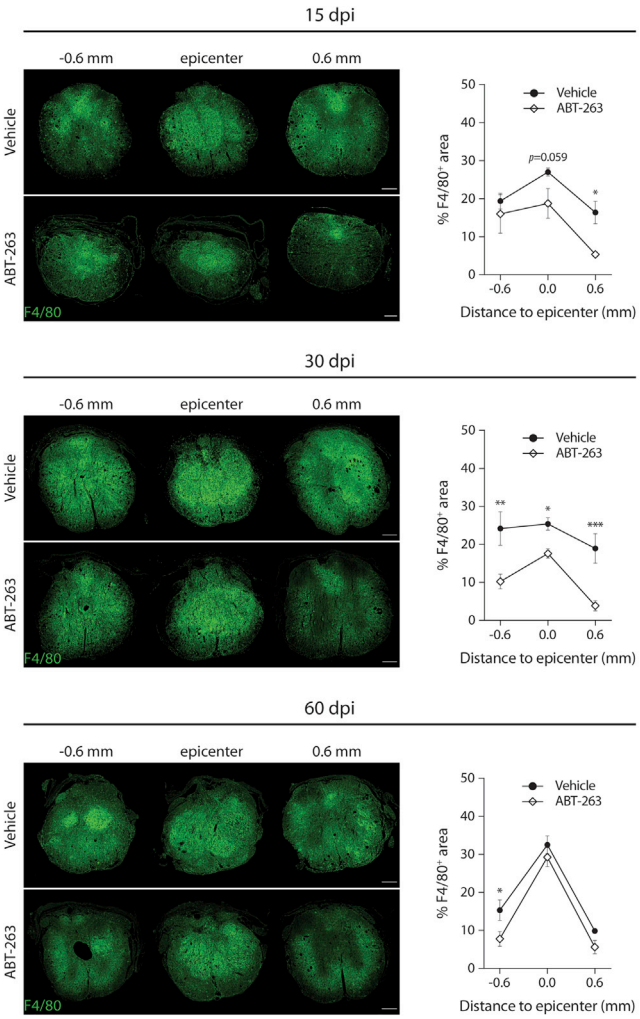

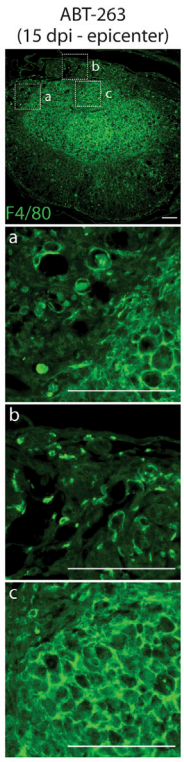

Figure 6. ABT-263 treatment decreases the number of macrophages at the injury site

Transversal sections at the lesion epicenter of an injured spinal cord at 15, 30 and 60 dpi treated with vehicle or ABT-263 and stained with the pan-macrophage marker F4/80 (green). Scale bars, 200 μm. The area of F4/80$^+$ tissue was measured at the lesion epicenter and 600 μm rostrally and caudally from the epicenter. The panel on the right displays zoomed images of three different zones (a–c) of an ABT-263-treated spinal cord transversal section stained with F4/80 at 15 dpi. Macrophages form a network inside the central lesion core, but they can be individually distinguished outside of it. Scale bars, 100 μm. Measurements are expressed as a percentage of the total cross-sectional area. n (15 dpi) = 3–4; n (30 dpi) = 3–4; n (60 dpi) = 2–3. Data are presented as mean ± SEM. *p < 0.05, **p < 0.01, ***p < 0.001, ABT-263 versus vehicle.

(PDGF)-BB, IGFBP-5, and Serpin E1, are strong mitogens and/or have been previously linked to fibrosis (Figure 7A). Notably, 14 out of 26 identified factors (e.g., IL-15, TNF-α, M-CSF, LIX, chemerin, I-TAC, and CCL11) are strong chemoattractant and/or pro-inflammatory agents (Figure 7B). Other factors, such as I-CAM, VCAM, and osteopontin, are involved in immune cell adhesion and migration (Figure 7C). Finally, CCL20, a known inducer of paracrine senescence, was reverted to pre-injury (sham) levels after ABT-263 treatment (Figure 7D), and CCL2, another stimulator of paracrine senescence, was greatly reduced in ABT-263-treated mice, although we could not find a significant upregulation upon injury. Of the 26 identified factors, 11 were previously described as SASP factors, namely amphiregulin, PDGF-BB, IGFBP-3, Serpin E1, IL-15, TNF-α, M-CSF, I-TAC, CCL11, ICAM-1, and CCL20 (Coppé et al., 2010).

These results provide mechanistic insights for the positive effects of ABT-263 on inflammation, fibrosis, and myelin preservation in the context of a spinal cord injury and are in line with our previous cellular analysis. Moreover, they reveal potential key SASP factors that contribute to the inhibitory microenvironment for repair in mammalian spinal cord injury settings.

DISCUSSION

The concepts of cellular senescence and their SASP have evolved remarkably during recent years. Yet, most of the mechanisms underlying the complexity of each senescent program remain unknown. While further studies are necessary to understand and reconcile the physiological and pathological roles of senescence, current knowledge favors the premise that transient and controlled induction of SCs is beneficial whereas accumulation and persistence of SCs is detrimental (Rhinn et al., 2019). Interestingly, the role of senescence in wound repair and organ regeneration contexts is still quite uncharted ground.

Herein, we describe the induction of SCs as a cellular response triggered by an injury in the spinal cord. These induced SCs exhibit several senescence features, including the co-expression of SA-β-gal with cell cycle inhibitors (namely p21 or p16) and the DNA damage marker γH2AX, as well as the absence of the proliferation marker BrdU. Our characterization is aligned with the three-step multi-marker system that has been recently proposed to identify SCs with more accuracy (Gorgoulis et al., 2019). Moreover, the significant accumulation of SA-β-gal$^+$ cells that we described at 15 dpi is consistent with the increased mRNA expression of p16, p21, and p53.

Our data show that most SCs, quantified in the gray matter located at the lesion periphery of injured spinal cords, are neurons. Post-mitotic neurons exhibiting several senescence features have already been described in the rat cortex in both rodent and human aging brains (Chinta et al., 2015; Jurk et al., 2012; Kang et al., 2015; Moreno-Blas et al., 2019; Walton and Andersen, 2019). Moreover, a recent study has demonstrated that senescent cortical neurons have their own SASP that is able to

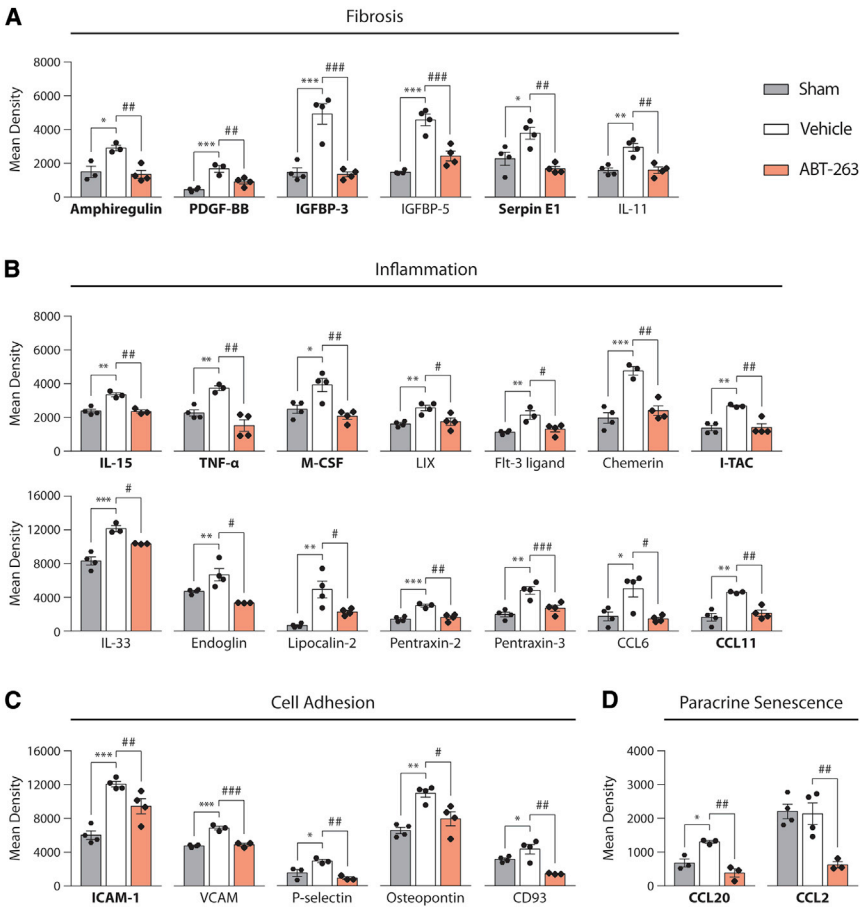

Figure 7. Targeting SCs with ABT-263 reduces key pro-inflammatory and pro-fibrotic factors that are induced upon spinal cord injury

(A–D) Cytokine and chemokine expression was measured in spinal cord homogenates from laminectomized (sham), vehicle-, and ABT-263-treated animals at 15 dpi. From a total of 111 factors analyzed, 26 were both upregulated upon injury (sham versus vehicle) and significantly decreased after ABT-263 treatment (vehicle versus ABT-263). Factors were divided in different groups regarding their role in (A) fibrosis, (B) inflammation, (C) cell adhesion, or (D) paracrine senescence. Some of the identified factors, displayed in bold, have been previously described as SASP factors. Data are expressed as mean density and presented as mean ± SEM. $^{*}p < 0.05$, $^{**}p < 0.01$, $^{***}p < 0.001$, vehicle versus sham; $^{\#}p < 0.05$, $^{\#\#}p < 0.01$, $^{\#\#\#}p < 0.001$, ABT-263 versus vehicle.

induce paracrine senescence in mouse embryonic fibroblasts (Moreno-Blas et al., 2019). We do not discard the possibility that other SC types, besides neurons, might also contribute to the pathophysiology of spinal cord injuries.

In the regenerative zebrafish model, SCs start to accumulate at the lesion periphery but are eventually cleared and returned to basal levels. This transient profile of SC induction seems to be a conserved injury response in organs with regenerative capacities, since it was also described in amputated appendages and damaged hearts of zebrafish, salamanders, and neonatal mice (Sarig et al., 2019; Da Silva-Álvarez et al., 2019; Yun et al., 2015). In the scarring mouse, however, the induced SCs persist at the lesion periphery and do not show any signs of being efficiently reduced over time. Albeit the outcome of zebrafish and mouse cellular responses to a spinal cord injury is different, the initial timing of major cellular events is similar between both models. Thus, even though we did not trace the senescence profile beyond 60 dpi, we argue that an inefficient clearance of SCs at early stages will contribute to the continuous increase of paracrine senescence alongside a chronic inflammatory environment, making the clearance of SCs from the mouse spinal cord highly improbable at later stages. This argument is in agreement with several studies in the field of senescence in which the inexistence of a timely clearance of SCs will result in the persistent propagation of chronic responses (Calcinotto et al., 2019; Rhinn et al., 2019). How are these transient versus persistent senescent profiles established is not known, but it is possible that these are associated with a specific SASP with different capacities to support a cell clearance mechanism. This seems to be the case in the salamander regenerative limb paradigm, where macrophages were shown to be an essential part of the mechanism that eliminates SCs (Yun et al., 2015). The functional demonstration of the positive role of transient SCs in a regenerative context comes from the observation that reducing SCs leads to a regeneration delay of amputated pectoral fins in zebrafish (Da Silva-Álvarez et al., 2019). These findings are in line with what was previously reported for skin wound healing, where transient SCs were found to be fundamental for tissue remodeling and repair (Demaria et al., 2014). In our hands, ABT-263 and two recently identified senolytic agents, ouabain and PF-573228 (Gil et al., 2018; Guerrero et al., 2019; Triana-Martínez et al., 2019), failed to target SCs in the zebrafish spinal cord using several different doses, vehicle solvents, and administration routes. Even though there is currently no tool to efficiently eliminate SCs in the zebrafish spinal cord, the observed transient profile suggests that a timely clearance of SCs might be required for proper regeneration to occur. In line with this idea, the persistent senescence profile we found in mice is compatible with the inability of mammals to regenerate the spinal cord after a lesion. Consequently, investigating the functional role of induced SCs after a spinal cord injury in mice became of paramount importance.

Senolytic drugs selectively eliminate SCs by transiently disabling the pro-survival networks and inducing their apoptosis (Zhu et al., 2015). One such drug is ABT-263, a specific inhibitor of anti-apoptotic proteins BCL-2 and BCL-xL (Zhu et al., 2016), already shown to selectively and efficiently kill SCs *in vivo* in

mice (Chang et al., 2016; Demaria et al., 2014). We used ABT-263 to reduce the number of SCs after a spinal cord T9 contusion injury in mice, and its effects on motor, sensory, and bladder function recovery were evaluated. We targeted the elimination of SCs in the subacute injury phase to guarantee that we were acting when macrophage infiltration, reactive astrogliosis, and scar formation are taking place (Siddiqui et al., 2015) but also to prevent their accumulation at the lesion periphery, which becomes statistically significant already at 15 dpi. We were able to show that SCs were decreased in injured mice treated with ABT-263, with targeting efficiencies similar to what was previously described (Demaria et al., 2014). Although the numbers of SCs are indeed reduced in all time points analyzed, they start to slowly re-emerge after the end of ABT-263 administration. This might be a consequence of paracrine senescence, a SASP-mediated event where the remaining SCs can induce senescence in nearby cells (Acosta et al., 2013). In fact, as a BCL-2/BCL-xL inhibitor, ABT-263 induces apoptosis in existent SCs, but it does not prevent the induction of new SCs. This becomes relevant when thinking in a translational approach where the administration time window should be carefully established for high efficacy with low toxicity.

The treatment of spinal-cord-injured mice with the senolytic ABT-263 significantly improved locomotor performance in BMS and HL tests, an effect maintained until the end of the study (i.e., 60 dpi), and also bladder function during the administration period. Interestingly, at 30 dpi, ABT-263-treated animals showed a normal sensitivity to a non-noxious cold stimulus, but no effects were observed upon a hot stimulus. This may indicate that SCs and their SASP are acting through specific neural substrates, namely through transient receptor potential member 8 (Trpm8) cation channels—primary molecular transducers of cold somatosensation (Ran et al., 2016).

Importantly, the effects of ABT-263 on locomotor and sensory recovery were corroborated by a second independent assay using the D+Q senolytic cocktail, known to exert its activity preferentially via phosphatidylinositol 3-kinase (PI3K) inhibition (Zhu et al., 2015). In addition, we could show that, similarly to ABT-263, the D+Q cocktail also resulted in an efficient depletion of SCs at the spinal cord lesion periphery. Taken together, these results highlight the detrimental impact of the persistent accumulation of SCs on motor and sensory functions after a spinal cord injury.

Persistent senescent fibroblasts and myogenic cells, through their SASP, were shown to promote a pro-fibrotic response and to limit tissue repair in fibrotic lung disease (Schafer et al., 2017) and injured muscles (Le Roux et al., 2015), respectively. Accordingly, we showed that the effect of ABT-263 on SCs depletion was translated into a consistently reduced fibrotic scar area and length. In addition, SCs depletion with ABT-263 results in a higher myelin preservation over time. While decreasing demyelination helps preserve the function of spared axons, a smaller scar provides a better microenvironment for the reorganization of spared axons around the lesion (Courtine and Sofroniew, 2019). Consistent with this scenario, ABT-263 treatment promoted an increased expression of the growth-associated GAP43 protein. Altogether, these effects are likely underlying the locomotor improvements observed.

The neuroinflammatory response after a spinal cord injury worsens throughout the secondary damage phase, becomes chronic, and is associated with neurotoxicity (Fleming et al., 2006). Preventing the accumulation of SCs during the subacute injury phase with the administration of ABT-263 led to a reduction in the number of inflammatory macrophages and concomitantly to a better functional outcome in injured mice. Interestingly, persistent SCs are known to create a chronic inflammatory tissue microenvironment by secreting pro-inflammatory cytokines such as IL-1α, IL-1β, M-CSF, or TNF-α, which are all well-established components of the SASP (Coppé et al., 2008, 2010). Moreover, neutralization of IL-1β and TNF-α signaling has already been shown to improve functional recovery after spinal cord injury (Genovese et al., 2008; Nesic et al., 2001). Indeed, our cytokine array identified M-CSF and TNF-α, two potent macrophage recruiters, as major factors upregulated after spinal cord injury and downregulated upon ABT-263 treatment.

The array analysis allowed us to identify crucial factors that may contribute to the inhibitory microenvironment for spinal cord repair and which expression is (at least partially) regulated by SCs. Amphiregulin has been demonstrated as a driver of tissue fibrosis but can also act as a pro-inflammatory agent (McKee et al., 2015; Perugorria et al., 2008; Yamane et al., 2008; Zaiss, 2020). PDGF and IGFBP factors, such as PDGF-BB and IGFBP-3/5, are widely recognized as strong mitogens for fibroblasts and are associated with fibrotic diseases (Lou et al., 2004; Nguyen et al., 2018; Pilewski et al., 2005; Trojanowska, 2008; Ying et al., 2017). Serpin E1, also known as plasminogen activator inhibitor-1 (PAI-1), is a known SASP factor that inhibits fibrinolysis and contributes to excess matrix deposition under pathological conditions (Ghosh and Vaughan, 2012). In turn, IL-11 signaling has been linked to chronic inflammation in fibrotic disease (Ng et al., 2020). Importantly, IGFBP-5, Serpin E1, and IL-11 were all shown to be upregulated after spinal cord injury (Cho et al., 2012; Hammarberg et al., 1998; Streeter et al., 2020; Zhang and Yang, 2017). The array pinpointed M-CSF and TNF-α, along with a plethora of other pro-inflammatory cytokines/chemokines, as key secreted factors that are upregulated by SCs upon mammalian spinal cord injury. These factors are either reduced or totally reverted to pre-injury (sham) levels after targeting SCs with ABT-263 during the subacute injury phase. This inflammatory group includes factors such as LIX, IL-33, endoglin, lipocalin-2, and CCL6, which have all been previously connected to spinal cord injury pathology (Glaser et al., 2004; Li et al., 2019; McTigue et al., 1998; Pomeshchik et al., 2015; Rathore et al., 2011). Thus, these factors establish a causal correlation between the persistent senescence profile and both the chronic inflammatory and fibrotic responses that result from a spinal cord injury.

Some of the identified factors are cell adhesion molecules, which play essential roles in the recruitment and migration of immune cells to the site of the injury during inflammation. Such is the case of ICAM-1, VCAM, P-selectin, and osteopontin, which have also been shown to be upregulated in spinal-cord-injured mice and/or human patients (Bao et al., 2004; Esposito et al., 2010; Hashimoto et al., 2003; Hu et al., 2015; Jing et al., 2014; Segal et al., 1997). In fact, ICAM-1/P-selectin-deficient mice

display improved functional recovery after injury (Farooque et al., 1999, 2001), while osteopontin-deficient mice exhibit less inflammation and significantly reduced area of spared white matter (Hashimoto et al., 2007).

Finally, one of the identified factors, CCL20, is a major mediator of paracrine senescence (Acosta et al., 2013). Curiously, antibody blockage of CCL20 has been reported to improve recovery after spinal cord injury (Hu et al., 2016). In addition, paracrine senescence has been shown to mediate the deleterious effects of SCs on disrupting tissue homeostasis and impairing organ regeneration (Campisi, 2005; Ferreira-Gonzalez et al., 2018). Therefore, the determination of a mediator of paracrine senescence and its downregulation upon targeting SCs with ABT-263 is crucial to comprehend the contributing role of senescence in mammalian spinal cord injury, especially how a senescence response can, if not controlled, spread itself across the spinal tissue. Moreover, the propagation of SASP responses throughout the tissue may explain the damage-signaling crosstalk between the lesion core and the lesion periphery.

It is noteworthy that the effects of ABT-263 seem to be more pronounced at the caudal side of the lesion. These differences in lesion responses to treatment suggest the existence of different SASP programs between the rostral and caudal sides. Although we did not explore such a possibility in our cytokine array, which was performed in a homogenate of both rostral and caudal tissue, this is something that may be worth further investigation in the future.

Our data provide evidence for the remarkable beneficial outcomes of targeting SCs in the context of a spinal cord injury, namely by reducing inflammation, limiting scarring, preserving myelin, and allowing axonal growth. This study presents compelling evidence that the accumulation of SCs after mammalian spinal cord injury is a major contributor to the inhibitory (pro-inflammatory and pro-fibrotic) microenvironment that compromises tissue repair and functional recovery. Targeted elimination of SCs emerges as a promising therapeutic approach to promote functional repair of an injured spinal cord, repurposing the use of senolytic therapies already under clinical trials for cancer and age-related disorders (Paez-Ribes et al., 2019). Given the extreme complexity and multifaceted mechanisms underlying spinal cord repair, it is important to acknowledge that, much like what happens with other therapies, a senolytic drug by itself may not be sufficient to generate clinically meaningful functional improvements. We do think, however, that the impact of senescence in the pathophysiology of spinal cord injuries should definitely be considered in future therapeutic strategies and that targeting SCs shows great potential to be combined with other existing biological and engineering approaches in a combinatorial therapeutic logic.

STAR★METHODS

Detailed methods are provided in the online version of this paper and include the following:

SUPPLEMENTAL INFORMATION

Supplemental information can be found online at https://doi.org/10.1016/j.celrep.2021.109334.

ACKNOWLEDGMENTS

We are grateful to A. Nascimento, A. Temudo, and J. Rino from the Bioimaging Unit for all of their precious advice. We thank the support given by the Fish and Rodent Facilities and the Histology and Comparative Pathology Laboratory, A. Ribeiro and C. de Sena-Tomás for critical reading of the manuscript, and M. Rebocho-da-Costa for help with the graphical abstract. D.P.d.C. was supported by a FCT PhD fellowship (PD/BD/105770/2014). I.M. was supported by a FCT post-doctoral fellowship (SFRH/BPD/118051/2016). A.M.C. was supported by a FCT fellowship (PTDC/BOM-MED/3295/2014). A.F.D. was supported by CONGENTO LISBOA-01-0145-FEDER-022170, co-financed by FCT (Portugal) and Lisboa2020, under the PORTUGAL2020 agreement (European Regional Development Fund). D.N.-S. was supported by a FCT PhD fellowship (SFRH/BD/138636/2018). D.C. was supported by a FCT PhD fellowship (PD/BD/114179/2016). L.S. was supported by a FCT IF contract. The project leading to these results has received funding from a FCT grant (PTDC/MED-NEU/30428/2017) and "la Caixa" Banking Foundation and FCT, I.P., under project code HR18-00187.

AUTHOR CONTRIBUTIONS

Conceptualization, L.S., A.J., and D.P.d.C.; methodology, L.S., D.P.d.C., and I.M.; investigation, D.P.d.C., I.M., A.M.C., A.F.D., D.N.-S., D.C., and A.F.; resources, T.P.; writing – original draft, D.P.d.C. and L.S.; writing – review & editing, D.P.d.C., L.S., I.M., and A.J.; visualization, D.P.d.C.; supervision, L.S. and A.J.; funding acquisition, L.S.

DECLARATION OF INTERESTS

D.P.d.C., I.M., A.J., and L.S. are inventors on an international patent (PCT/EP2020/075769, "Treatment of spinal cord injury") submitted by Instituto de

Medicina Molecular – João Lobo Antunes and Universidade Nova de Lisboa. The remaining authors declare no competing interests.

Received: September 8, 2020
Revised: March 31, 2021
Accepted: June 10, 2021
Published: July 6, 2021

SUPPORTING CITATIONS

The following references appear in the supplemental information: Farr et al., 2016, Ghatei et al., 2017, Langnaese et al., 2008.

REFERENCES

Acosta, J.C., Banito, A., Wuestefeld, T., Georgilis, A., Janich, P., Morton, J.P., Athineos, D., Kang, T.-W., Lasitschka, F., Andrulis, M., et al. (2013). A complex secretory program orchestrated by the inflammasome controls paracrine senescence. Nat. Cell Biol. *15*, 978–990.

Almutiri, S., Berry, M., Logan, A., and Ahmed, Z. (2018). Non-viral-mediated suppression of AMIGO3 promotes disinhibited NT3-mediated regeneration of spinal cord dorsal column axons. Sci. Rep. *8*, 10707.

Bao, F., Chen, Y., Dekaban, G.A., and Weaver, L.C. (2004). Early anti-inflammatory treatment reduces lipid peroxidation and protein nitration after spinal cord injury in rats. J. Neurochem. *88*, 1335–1344.

Basso, D.M., Fisher, L.C., Anderson, A.J., Jakeman, L.B., McTigue, D.M., and Popovich, P.G. (2006). Basso Mouse Scale for locomotion detects differences in recovery after spinal cord injury in five common mouse strains. J. Neurotrauma *23*, 635–659.

Beck, K.D., Nguyen, H.X., Galvan, M.D., Salazar, D.L., Woodruff, T.M., and Anderson, A.J. (2010). Quantitative analysis of cellular inflammation after traumatic spinal cord injury: Evidence for a multiphasic inflammatory response in the acute to chronic environment. Brain *133*, 433–447.

Becker, T., Wullimann, M.F., Becker, C.G., Bernhardt, R.R., and Schachner, M. (1997). Axonal regrowth after spinal cord transection in adult zebrafish. J. Comp. Neurol. *377*, 577–595.

Benowitz, L.I., and Routtenberg, A. (1987). A membrane phosphoprotein associated with neural development, axonal regeneration, phospholipid metabolism, and synaptic plasticity. Trends Neurosci. *10*, 527–532.

Blight, A.R. (1985). Delayed demyelination and macrophage invasion: A candidate for secondary cell damage in spinal cord injury. Cent. Nerv. Syst. Trauma *2*, 299–315.

Brennan, F.H., and Popovich, P.G. (2018). Emerging targets for reprograming the immune response to promote repair and recovery of function after spinal cord injury. Curr. Opin. Neurol. *31*, 334–344.

Calcinotto, A., Kohli, J., Zagato, E., Pellegrini, L., Demaria, M., and Alimonti, A. (2019). Cellular senescence: Aging, cancer, and injury. Physiol. Rev. *99*, 1047–1078.

Campisi, J. (2005). Senescent cells, tumor suppression, and organismal aging: Good citizens, bad neighbors. Cell *120*, 513–522.

Campisi, J. (2013). Aging, cellular senescence, and cancer. Annu. Rev. Physiol. *75*, 685–705.

Chang, J., Wang, Y., Shao, L., Laberge, R.-M., Demaria, M., Campisi, J., Janakiraman, K., Sharpless, N.E., Ding, S., Feng, W., et al. (2016). Clearance of senescent cells by ABT263 rejuvenates aged hematopoietic stem cells in mice. Nat. Med. *22*, 78–83.

Childs, B.G., Durik, M., Baker, D.J., and van Deursen, J.M. (2015). Cellular senescence in aging and age-related disease: From mechanisms to therapy. Nat. Med. *21*, 1424–1435.

Chinta, S.J., Woods, G., Rane, A., Demaria, M., Campisi, J., and Andersen, J.K. (2015). Cellular senescence and the aging brain. Exp. Gerontol. *68*, 3–7.

Cho, N., Nguyen, D.H., Satkunendrarajah, K., Branch, D.R., and Fehlings, M.G. (2012). Evaluating the role of IL-11, a novel cytokine in the IL-6 family, in a mouse model of spinal cord injury. J. Neuroinflammation *9*, 134.

Coppé, J.-P., Patil, C.K., Rodier, F., Sun, Y., Muñoz, D.P., Goldstein, J., Nelson, P.S., Desprez, P.-Y., and Campisi, J. (2008). Senescence-associated secretory phenotypes reveal cell-nonautonomous functions of oncogenic RAS and the p53 tumor suppressor. PLoS Biol. *6*, 2853–2868.

Coppé, J.-P., Desprez, P.-Y., Krtolica, A., and Campisi, J. (2010). The senescence-associated secretory phenotype: The dark side of tumor suppression. Annu. Rev. Pathol. *5*, 99–118.

Courtine, G., and Sofroniew, M.V. (2019). Spinal cord repair: Advances in biology and technology. Nat. Med. *25*, 898–908.

Cregg, J.M., DePaul, M.A., Filous, A.R., Lang, B.T., Tran, A., and Silver, J. (2014). Functional regeneration beyond the glial scar. Exp. Neurol. *253*, 197–207.

Crowe, M.J., Bresnahan, J.C., Shuman, S.L., Masters, J.N., and Beattie, M.S. (1997). Apoptosis and delayed degeneration after spinal cord injury in rats and monkeys. Nat. Med. *3*, 73–76.

Cummings, B.J., Engesser-Cesar, C., Cadena, G., and Anderson, A.J. (2007). Adaptation of a ladder beam walking task to assess locomotor recovery in mice following spinal cord injury. Behav. Brain Res. *177*, 232–241.

Da Silva-Álvarez, S., Guerra-Varela, J., Sobrido-Cameán, D., Quelle, A., Barreiro-Iglesias, A., Sánchez, L., and Collado, M. (2019). Cell senescence contributes to tissue regeneration in zebrafish. Aging Cell *19*, e13052.

Demaria, M., Ohtani, N., Youssef, S.A., Rodier, F., Toussaint, W., Mitchell, J.R., Laberge, R.-M., Vijg, J., Van Steeg, H., Dollé, M.E.T., et al. (2014). An essential role for senescent cells in optimal wound healing through secretion of PDGF-AA. Dev. Cell *31*, 722–733.

Dias, D.O., Kim, H., Holl, D., Werne Solnestam, B., Lundeberg, J., Carlén, M., Göritz, C., and Frisén, J. (2018). Reducing pericyte-derived scarring promotes recovery after spinal cord injury. Cell *173*, 153–165.e22.

Donnelly, D.J., and Popovich, P.G. (2008). Inflammation and its role in neuroprotection, axonal regeneration and functional recovery after spinal cord injury. Exp. Neurol. *209*, 378–388.

Emery, E., Aldana, P., Bunge, M.B., Puckett, W., Srinivasan, A., Keane, R.W., Bethea, J., and Levi, A.D.O. (1998). Apoptosis after traumatic human spinal cord injury. J. Neurosurg. *89*, 911–920.

Esposito, E., Mazzon, E., Paterniti, I., Impellizzeri, D., Bramanti, P., and Cuzzocrea, S. (2010). Olprinone attenuates the acute inflammatory response and apoptosis after spinal cord trauma in mice. PLoS ONE *5*, e12170.

Fang, P., Lin, J.-F., Pan, H.-C., Shen, Y.-Q., and Schachner, M. (2012). A surgery protocol for adult zebrafish spinal cord injury. J. Genet. Genomics *39*, 481–487.

Farooque, M., Isaksson, J., and Olsson, Y. (1999). Improved recovery after spinal cord trauma in ICAM-1 and P-selectin knockout mice. Neuroreport *10*, 131–134.

Farooque, M., Isaksson, J., and Olsson, Y. (2001). White matter preservation after spinal cord injury in ICAM-1/P-selectin-deficient mice. Acta Neuropathol. *102*, 132–140.

Farr, J.N., Fraser, D.G., Wang, H., Jaehn, K., Ogrodnik, M.B., Weivoda, M.M., Drake, M.T., Tchkonia, T., LeBrasseur, N.K., Kirkland, J.L., et al. (2016). Identification of senescent cells in the bone microenvironment. J. Bone Miner. Res. *31*, 1920–1929.

Ferreira-Gonzalez, S., Lu, W.-Y., Raven, A., Dwyer, B., Man, T.Y., O'Duibhir, E., Lewis, P.J.S., Campana, L., Kendall, T.J., Bird, T.G., et al. (2018). Paracrine cellular senescence exacerbates biliary injury and impairs regeneration. Nat. Commun. *9*, 1020.

Fitch, M.T., and Silver, J. (1997). Activated macrophages and the blood-brain barrier: Inflammation after CNS injury leads to increases in putative inhibitory molecules. Exp. Neurol. *148*, 587–603.

Fleming, J.C., Norenberg, M.D., Ramsay, D.A., Dekaban, G.A., Marcillo, A.E., Saenz, A.D., Pasquale-Styles, M., Dietrich, W.D., and Weaver, L.C. (2006). The cellular inflammatory response in human spinal cords after injury. Brain *129*, 3249–3269.

Genovese, T., Mazzon, E., Crisafulli, C., Di Paola, R., Muià, C., Esposito, E., Bramanti, P., and Cuzzocrea, S. (2008). TNF-α blockage in a mouse model of SCI: Evidence for improved outcome. Shock *29*, 32–41.

Ghatei, N., Nabavi, A.S., Toosi, M.H.B., Azimian, H., Homayoun, M., Targhi, R.G., and Haghir, H. (2017). Evaluation of *bax*, *bcl-2*, *p21* and *p53* genes expression variations on cerebellum of BALB/c mice before and after birth under mobile phone radiation exposure. Iran. J. Basic Med. Sci. *20*, 1037–1043.

Ghosh, A.K., and Vaughan, D.E. (2012). PAI-1 in tissue fibrosis. J. Cell. Physiol. *227*, 493–507.

Gil, J., Guerrero, A., and Harranz, N. (2018). Semolytic compounds. International patent application publication WO2018215795A2, published November 29, 2018-05-25.

Glaser, J., Gonzalez, R., Perreau, V.M., Cotman, C.W., and Keirstead, H.S. (2004). Neutralization of the chemokine CXCL10 enhances tissue sparing and angiogenesis following spinal cord injury. J. Neurosci. Res. *77*, 701–708.

Gorgoulis, V., Adams, P.D., Alimonti, A., Bennett, D.C., Bischof, O., Bishop, C., Campisi, J., Collado, M., Evangelou, K., Ferbeyre, G., et al. (2019). Cellular senescence: Defining a path forward. Cell *179*, 813–827.

Guerrero, A., Herranz, N., Sun, B., Wagner, V., Gallage, S., Guiho, R., Wolter, K., Pombo, J., Irvine, E.E., Innes, A.J., et al. (2019). Cardiac glycosides are broad-spectrum senolytics. Nat. Metab. *1*, 1074–1088.

Hammarberg, H., Risling, M., Hökfelt, T., Cullheim, S., and Piehl, F. (1998). Expression of insulin-like growth factors and corresponding binding proteins (IGFBP 1-6) in rat spinal cord and peripheral nerve after axonal injuries. J. Comp. Neurol. *400*, 57–72.

Harrison, M., O'Brien, A., Adams, L., Cowin, G., Ruitenberg, M.J., Sengul, G., and Watson, C. (2013). Vertebral landmarks for the identification of spinal cord segments in the mouse. Neuroimage *68*, 22–29.

Hashimoto, M., Koda, M., Ino, H., Murakami, M., Yamazaki, M., and Moriya, H. (2003). Upregulation of osteopontin expression in rat spinal cord microglia after traumatic injury. J. Neurotrauma *20*, 287–296.

Hashimoto, M., Sun, D., Rittling, S.R., Denhardt, D.T., and Young, W. (2007). Osteopontin-deficient mice exhibit less inflammation, greater tissue damage, and impaired locomotor recovery from spinal cord injury compared with wild-type controls. J. Neurosci. *27*, 3603–3611.

Hata, K., Fujitani, M., Yasuda, Y., Doya, H., Saito, T., Yamagishi, S., Mueller, B.K., and Yamashita, T. (2006). RGMa inhibition promotes axonal growth and recovery after spinal cord injury. J. Cell Biol. *173*, 47–58.

Herranz, N., and Gil, J. (2018). Mechanisms and functions of cellular senescence. J. Clin. Invest. *128*, 1238–1246.

Hu, J., Zeng, L., Huang, J., Wang, G., and Lu, H. (2015). miR-126 promotes angiogenesis and attenuates inflammation after contusion spinal cord injury in rats. Brain Res. *1608*, 191–202.

Hu, J., Yang, Z., Li, X., and Lu, H. (2016). C-C motif chemokine ligand 20 regulates neuroinflammation following spinal cord injury via Th17 cell recruitment. J. Neuroinflammation *13*, 162.

Itahana, K., Campisi, J., and Dimri, G.P. (2007). Methods to detect biomarkers of cellular senescence: The senescence-associated β-galactosidase assay. Methods Mol. Biol. *371*, 21–31.

Jing, Y., Wu, Q., Yuan, X., Li, B., Liu, M., Zhang, X., Liu, S., Li, H., and Xiu, R. (2014). Microvascular protective role of pericytes in melatonin-treated spinal cord injury in the C57BL/6 mice. Chin. Med. J. (Engl.) *127*, 2808–2813.

Jun, J.-I., and Lau, L.F. (2010). The matricellular protein CCN1 induces fibroblast senescence and restricts fibrosis in cutaneous wound healing. Nat. Cell Biol. *12*, 676–685.

Jurk, D., Wang, C., Miwa, S., Maddick, M., Korolchuk, V., Tsolou, A., Gonos, E.S., Thrasivoulou, C., Saffrey, M.J., Cameron, K., and von Zglinicki, T. (2012). Postmitotic neurons develop a p21-dependent senescence-like phenotype driven by a DNA damage response. Aging Cell *11*, 996–1004.

Kang, C., Xu, Q., Martin, T.D., Li, M.Z., Demaria, M., Aron, L., Lu, T., Yankner, B.A., Campisi, J., and Elledge, S.J. (2015). The DNA damage response induces inflammation and senescence by inhibiting autophagy of GATA4. Science *349*, aaa5612.

Kong, X., Feng, D., Wang, H., Hong, F., Bertola, A., Wang, F.-S., and Gao, B. (2012). Interleukin-22 induces hepatic stellate cell senescence and restricts liver fibrosis in mice. Hepatology *56*, 1150–1159.

Krizhanovsky, V., Yon, M., Dickins, R.A., Hearn, S., Simon, J., Miething, C., Yee, H., Zender, L., and Lowe, S.W. (2008). Senescence of activated stellate cells limits liver fibrosis. Cell *134*, 657–667.

Krtolica, A., Parrinello, S., Lockett, S., Desprez, P.-Y., and Campisi, J. (2001). Senescent fibroblasts promote epithelial cell growth and tumorigenesis: A link between cancer and aging. Proc. Natl. Acad. Sci. USA *98*, 12072–12077.

Langnaese, K., John, R., Schweizer, H., Ebmeyer, U., and Keilhoff, G. (2008). Selection of reference genes for quantitative real-time PCR in a rat asphyxial cardiac arrest model. BMC Mol. Biol. *9*, 53.

Le Roux, I., Konge, J., Le Cam, L., Flamant, P., and Tajbakhsh, S. (2015). Numb is required to prevent p53-dependent senescence following skeletal muscle injury. Nat. Commun. *6*, 8528.

Li, Y., Chen, Y., Li, X., Wu, J., Pan, J.-Y., Cai, R.-X., Yang, R.-Y., and Wang, X.-D. (2019). RNA sequencing screening of differentially expressed genes after spinal cord injury. Neural Regen. Res. *14*, 1583–1593.

Lou, S.-M., Li, Y.-M., Wang, K.-M., Cai, W.-M., and Weng, H.-L. (2004). Expression of platelet-derived growth factor-BB in liver tissues of patients with chronic hepatitis B. World J. Gastroenterol. *10*, 385–388.

Mason, M.R.J., Lieberman, A.R., Grenningloh, G., and Anderson, P.N. (2002). Transcriptional upregulation of SCG10 and CAP-23 is correlated with regeneration of the axons of peripheral and central neurons in vivo. Mol. Cell. Neurosci. *20*, 595–615.

McKee, C., Sigala, B., Soeda, J., Mouralidarane, A., Morgan, M., Mazzoccoli, G., Rappa, F., Cappello, F., Cabibi, D., Pazienza, V., et al. (2015). Amphiregulin activates human hepatic stellate cells and is upregulated in non alcoholic steatohepatitis. Sci. Rep. *5*, 8812.

McTigue, D.M., Tani, M., Krivacic, K., Chernosky, A., Kelner, G.S., Maciejewski, D., Maki, R., Ransohoff, R.M., and Stokes, B.T. (1998). Selective chemokine mRNA accumulation in the rat spinal cord after contusion injury. J. Neurosci. Res. *53*, 368–376.

Meyer, K., Hodwin, B., Ramanujam, D., Engelhardt, S., and Sarikas, A. (2016). Essential role for premature senescence of myofibroblasts in myocardial fibrosis. J. Am. Coll. Cardiol. *67*, 2018–2028.

Moreno-Blas, D., Gorostieta-Salas, E., Pommer-Alba, A., Muciño-Hernández, G., Gerónimo-Olvera, C., Maciel-Barón, L.A., Konigsberg, M., Massieu, L., and Castro-Obregón, S. (2019). Cortical neurons develop a senescence-like phenotype promoted by dysfunctional autophagy. Aging (Albany NY) *11*, 6175–6198.

Nakae, A., Nakai, K., Yano, K., Hosokawa, K., Shibata, M., and Mashimo, T. (2011). The animal model of spinal cord injury as an experimental pain model. J. Biomed. Biotechnol. *2011*, 939023.

Narita, M., Nũnez, S., Heard, E., Narita, M., Lin, A.W., Hearn, S.A., Spector, D.L., Hannon, G.J., and Lowe, S.W. (2003). Rb-mediated heterochromatin formation and silencing of E2F target genes during cellular senescence. Cell *113*, 703–716.

Nesic, O., Xu, G.-Y., McAdoo, D., High, K.W., Hulsebosch, C., and Perez-Pol, R. (2001). IL-1 receptor antagonist prevents apoptosis and caspase-3 activation after spinal cord injury. J. Neurotrauma *18*, 947–956.

Ng, B., Cook, S.A., and Schafer, S. (2020). Interleukin-11 signaling underlies fibrosis, parenchymal dysfunction, and chronic inflammation of the airway. Exp. Mol. Med. *52*, 1871–1878.

Nguyen, X.-X., Muhammad, L., Nietert, P.J., and Feghali-Bostwick, C. (2018). IGFBP-5 promotes fibrosis via increasing its own expression and that of other pro-fibrotic mediators. Front. Endocrinol. (Lausanne) *9*, 601.

O'Shea, T.M., Burda, J.E., and Sofroniew, M.V. (2017). Cell biology of spinal cord injury and repair. J. Clin. Invest. *127*, 3259–3270.

Paez-Ribes, M., González-Gualda, E., Doherty, G.J., and Muñoz-Espín, D. (2019). Targeting senescent cells in translational medicine. EMBO Mol. Med. *11*, e10234.

Perugorria, M.J., Latasa, M.U., Nicou, A., Cartagena-Lirola, H., Castillo, J., Goñi, S., Vespasiani-Gentilucci, U., Zagami, M.G., Lotersztajn, S., Prieto, J., et al. (2008). The epidermal growth factor receptor ligand amphiregulin participates in the development of mouse liver fibrosis. Hepatology *48*, 1251–1261.

Pilewski, J.M., Liu, L., Henry, A.C., Knauer, A.V., and Feghali-Bostwick, C.A. (2005). Insulin-like growth factor binding proteins 3 and 5 are overexpressed in idiopathic pulmonary fibrosis and contribute to extracellular matrix deposition. Am. J. Pathol. *166*, 399–407.

Pomeshchik, Y., Kidin, I., Korhonen, P., Savchenko, E., Jaronen, M., Lehtonen, S., Wojciechowski, S., Kanninen, K., Koistinaho, J., and Malm, T. (2015). Interleukin-33 treatment reduces secondary injury and improves functional recovery after contusion spinal cord injury. Brain Behav. Immun. *44*, 68–81.

Popovich, P.G., Wei, P., and Stokes, B.T. (1997). Cellular inflammatory response after spinal cord injury in Sprague-Dawley and Lewis rats. J. Comp. Neurol. *377*, 443–464.

Popovich, P.G., Guan, Z., Wei, P., Huitinga, I., van Rooijen, N., and Stokes, B.T. (1999). Depletion of hematogenous macrophages promotes partial hindlimb recovery and neuroanatomical repair after experimental spinal cord injury. Exp. Neurol. *158*, 351–365.

Ran, C., Hoon, M.A., and Chen, X. (2016). The coding of cutaneous temperature in the spinal cord. Nat. Neurosci. *19*, 1201–1209.

Rathore, K.I., Berard, J.L., Redensek, A., Chierzi, S., Lopez-Vales, R., Santos, M., Akira, S., and David, S. (2011). Lipocalin 2 plays an immunomodulatory role and has detrimental effects after spinal cord injury. J. Neurosci. *31*, 13412–13419.

Rhinn, M., Ritschka, B., and Keyes, W.M. (2019). Cellular senescence in development, regeneration and disease. Development *146*, dev151837.

Sarig, R., Rimmer, R., Bassat, E., Zhang, L., Umansky, K.B., Lendengolts, D., Perlmoter, G., Yaniv, K., and Tzahor, E. (2019). Transient p53-mediated regenerative senescence in the injured heart. Circulation *139*, 2491–2494.

Schafer, M.J., White, T.A., Iijima, K., Haak, A.J., Ligresti, G., Atkinson, E.J., Oberg, A.L., Birch, J., Salmonowicz, H., Zhu, Y., et al. (2017). Cellular senescence mediates fibrotic pulmonary disease. Nat. Commun. *8*, 14532.

Scheff, S.W., Rabchevsky, A.G., Fugaccia, I., Main, J.A., and Lumpp, J.E., Jr. (2003). Experimental modeling of spinal cord injury: Characterization of a force-defined injury device. J. Neurotrauma *20*, 179–193.

Schindelin, J., Arganda-Carreras, I., Frise, E., Kaynig, V., Longair, M., Pietzsch, T., Preibisch, S., Rueden, C., Saalfeld, S., Schmid, B., et al. (2012). Fiji: an open-source platform for biological-image analysis. Nature Methods *9*, 676–682.

Segal, J.L., Gonzales, E., Yousefi, S., Jamshidipour, L., and Brunnemann, S.R. (1997). Circulating levels of IL-2R, ICAM-1, and IL-6 in spinal cord injuries. Arch. Phys. Med. Rehabil. *78*, 44–47.

Siddiqui, A.M., Khazaei, M., and Fehlings, M.G. (2015). Translating mechanisms of neuroprotection, regeneration, and repair to treatment of spinal cord injury. Prog. Brain Res *218*, 15–54.

Soderblom, C., Luo, X., Blumenthal, E., Bray, E., Lyapichev, K., Ramos, J., Krishnan, V., Lai-Hsu, C., Park, K.K., Tsoulfas, P., et al. (2013). Perivascular fibroblasts form the fibrotic scar after contusive spinal cord injury. J. Neurosci. *33*, 13882–13887.

Streeter, K.A., Sunshine, M.D., Brant, J.O., Sandoval, A.G.W., Maden, M., and Fuller, D.D. (2020). Molecular and histologic outcomes following spinal cord injury in spiny mice, *Acomys cahirinus*. J. Comp. Neurol. *528*, 1535–1547.

Totoiu, M.O., and Keirstead, H.S. (2005). Spinal cord injury is accompanied by chronic progressive demyelination. J. Comp. Neurol. *486*, 373–383.

Triana-Martínez, F., Picallos-Rabina, P., Da Silva-Álvarez, S., Pietrocola, F., Llanos, S., Rodilla, V., Soprano, E., Pedrosa, P., Ferreirós, A., Barradas, M., et al. (2019). Identification and characterization of cardiac glycosides as senolytic compounds. Nat. Commun. *10*, 4731.

Trojanowska, M. (2008). Role of PDGF in fibrotic diseases and systemic sclerosis. Rheumatology (Oxford) *47* (*Suppl 5*), v2–v4.

Tsarouchas, T.M., Wehner, D., Cavone, L., Munir, T., Keatinge, M., Lambertus, M., Underhill, A., Barrett, T., Kassapis, E., Ogryzko, N., et al. (2018). Dynamic control of proinflammatory cytokines Il-1β and Tnf-α by macrophages in zebrafish spinal cord regeneration. Nat. Commun. *9*, 4670.

Vajn, K., Plunkett, J.A., Tapanes-Castillo, A., and Oudega, M. (2013). Axonal regeneration after spinal cord injury in zebrafish and mammals: differences, similarities, translation. Neurosci. Bull. *29*, 402–410.

van Deursen, J.M. (2014). The role of senescent cells in ageing. Nature *509*, 439–446.

Walton, C.C., and Andersen, J.K. (2019). Unknown fates of (brain) oxidation or UFO: Close encounters with neuronal senescence. Free Radic. Biol. Med. *134*, 695–701.

Watson, J.L., Hala, T.J., Putatunda, R., Sannie, D., and Lepore, A.C. (2014). Persistent at-level thermal hyperalgesia and tactile allodynia accompany chronic neuronal and astrocyte activation in superficial dorsal horn following mouse cervical contusion spinal cord injury. PLoS ONE *9*, e109099.

Whetstone, W.D., Hsu, J.-Y.C., Eisenberg, M., Werb, Z., and Noble-Haeusslein, L.J. (2003). Blood-spinal cord barrier after spinal cord injury: Relation to revascularization and wound healing. J. Neurosci. Res. *74*, 227–239.

Yalcin, I., Charlet, A., Freund-Mercier, M.-J., Barrot, M., and Poisbeau, P. (2009). Differentiating thermal allodynia and hyperalgesia using dynamic hot and cold plate in rodents. J. Pain *10*, 767–773.

Yamane, S., Ishida, S., Hanamoto, Y., Kumagai, K., Masuda, R., Tanaka, K., Shiobara, N., Yamane, N., Mori, T., Juji, T., et al. (2008). Proinflammatory role of amphiregulin, an epidermal growth factor family member whose expression is augmented in rheumatoid arthritis patients. J. Inflamm. (Lond.) *5*, 5.

Ying, H.-Z., Chen, Q., Zhang, W.-Y., Zhang, H.-H., Ma, Y., Zhang, S.-Z., Fang, J., and Yu, C.-H. (2017). PDGF signaling pathway in hepatic fibrosis pathogenesis and therapeutics (Review). Mol. Med. Rep. *16*, 7879–7889.

Yoshimura, N. (1999). Bladder afferent pathway and spinal cord injury: Possible mechanisms inducing hyperreflexia of the urinary bladder. Prog. Neurobiol. *57*, 583–606.

Yun, M.H., Davaapil, H., and Brockes, J.P. (2015). Recurrent turnover of senescent cells during regeneration of a complex structure. eLife *4*, e05505.

Zaiss, D.M.W. (2020). Amphiregulin as a driver of tissue fibrosis. Am. J. Transplant. *20*, 631–632.

Zhang, G., and Yang, P. (2017). Bioinformatics genes and pathway analysis for chronic neuropathic pain after spinal cord injury. BioMed Res. Int. *2017*, 6423021.

Zhu, Y., Tchkonia, T., Pirtskhalava, T., Gower, A.C., Ding, H., Giorgadze, N., Palmer, A.K., Ikeno, Y., Hubbard, G.B., Lenburg, M., et al. (2015). The Achilles' heel of senescent cells: from transcriptome to senolytic drugs. Aging Cell *14*, 644–658.

Zhu, Y., Tchkonia, T., Fuhrmann-Stroissnigg, H., Dai, H.M., Ling, Y.Y., Stout, M.B., Pirtskhalava, T., Giorgadze, N., Johnson, K.O., Giles, C.B., et al. (2016). Identification of a novel senolytic agent, navitoclax, targeting the Bcl-2 family of anti-apoptotic factors. Aging Cell *15*, 428–435.

STAR★METHODS

KEY RESOURCES TABLE

REAGENT or RESOURCE	SOURCE	IDENTIFIER
Antibodies		
Rabbit anti-p21	Santa Cruz	Cat#sc-397; RRID: AB_632126
Mouse anti-BrdU	Sigma	Cat#B2531; RRID: AB_476793
Rabbit anti-γH2AX	Novus Biologicals	Cat#NB100-384; RRID: AB_10002815
Rabbit anti-p16	ProteIntech	Cat#10883-1-AP; RRID: AB_2078303
Mouse anti-HuC/D	Life Technologies	Cat#A21271; RRID: AB_221448
Rabbit anti-NeuN	ProteIntech	Cat#26975-1-AP; RRID: AB_2880708
Rat anti-GFAP	ThermoFisher Scientific	Cat#13-0300; RRID: AB_2532994
Rabbit anti-PDGFRβ	Abcam	Cat#ab32570; RRID: AB_777165
Rat anti-F4/80	Abcam	Cat#ab6640; RRID: AB_1140040
Rabbit anti-GAP43	Novus Biologicals	Cat#NB300-143; RRID: AB_10001196
Mouse anti-GADPH	ThermoFisher Scientific	Cat#AM4300; RRID: AB_2536381
Goat anti-rabbit Alexa Fluor 488	ThermoFisher Scientific	Cat#A11008; RRID: AB_143165
Goat anti-rabbit Alexa Fluor 568	ThermoFisher Scientific	Cat#A11011; RRID: AB_143157
Goat anti-rat Alexa Fluor 488	ThermoFisher Scientific	Cat#A11006; RRID: AB_141373
Goat anti-mouse Alexa Fluor 594	ThermoFisher Scientific	Cat#A11020; RRID: AB_141974
Chemicals, peptides, and recombinant proteins		
ABT-263	Selleckchem	Cat#S1001; CAS: 923564-51-6
Dasatinib	Sigma	Cat#SML2589; CAS: 302962-49-8
Quercetin	Sigma	Cat#1592409; CAS: 6151-25-3
Corn oil	Sigma	Cat#C8267; CAS: 8001-30-7
PEG400	Sigma	Cat#81172; CAS: 25322-68-3
Tricaine	Sigma	Cat#MS222; CAS: 886-86-2
Gelatin	Sigma	Cat#G6144; CAS: 9000-70-8
DAPI	Sigma	Cat#D9564
FluoroMyelin™ Green	ThermoFisher Scientific	Cat#F34651
Critical commercial assays		
SA-β-gal assay kit	Cell Signaling	Cat#9860
Proteome Profiler Mouse XL Cytokine Array	R&D Systems	Cat#ARY028
Experimental models: Organisms/strains		
Mouse: C57BL/6J	Charles River Laboratory	RRID:IMSR_JAX:000664
Zebrafish	ZIRC	Cat#ZL1; ZFIN ID: ZDB-LAB-991005-53
Oligonucleotides		
Primers for qPCR, see Table S2	This paper	N/A
Software and algorithms		
Fiji	Herranz and	https://imagej.nih.gov/ij/
GraphPad Prism	GraphPad Software	V7.00
Sigmaplot	Systat Software Inc	V14.0
ZEN 2	Zeiss	Blue edition
Adobe Illustrator	Adobe	https://www.adobe.com/
Image Studio Lite	LI-COR	V5.2

RESOURCE AVAILABILITY

Lead contact

Further information and requests for resources and reagents should be directed to and will be fulfilled by the Lead Contact, Leonor Saúde (msaude@medicina.ulisboa.pt).

Materials availability

This study did not generate new unique reagents.

Data and code availability

This study did not generate any datasets/code.

EXPERIMENTAL MODEL AND SUBJECT DETAILS

Ethics statement

All handling, surgical and post-operative care procedures were approved by Instituto de Medicina Molecular Internal Committee (ORBEA) and the Portuguese Animal Ethics Committee (DGAV), in accordance with the European Community guidelines (Directive 2010/63/EU) and the Portuguese law on animal care (DL 113/2013). All efforts were made to minimize the number of animals used and to decrease suffering of the animals used in the study.

Zebrafish

AB strain zebrafish (*Danio rerio*) were obtained from Zebrafish International Resource Center (ZIRC). Animals were bred, grown and maintained on a 14-hour/10-hour light/dark cycle at 28°C following the standard guidelines for fish care and maintenance protocols. Adult (3-6 months old) male and female fish were used in the experiments.

Mouse

Adult (8-9 weeks old) female C57BL/6J mice (*Mus musculus*) were purchased from Charles River Laboratory. Animals were housed in the Instituto de Medicina Molecular animal facility under conventional conditions on a 12-hour light-dark cycle with *ad libitum* access to food and water. 10-11 weeks old mice were used in the experiments.

Study design

Rationale and experimental design

This study was designed to investigate the role of senescence in a spinal cord injury context. Standard senescence biomarkers (SA-β-gal, $p21^{CIP1}$, $p16^{INK4a}$ and γH2AX) were used to characterize SCs induced after injury. We used ABT-263, a drug with powerful senolytic activity, to pharmacologically deplete SCs during the sub-acute phase of the injury. BMS and HL tests were used to study locomotor recovery, while the ITP assessed sensory function. At the cellular level, we evaluated the impact of targeting SCs on myelin and axonal preservation, fibrosis and inflammation. A cytokine array was performed in order to identify potential factors secreted by SCs that may contribute to inhibitory microenvironment for repair after spinal cord injury.

Randomization and blinding

After the injury, animals were randomly assigned to each experimental group and end-point. Experimenters were blinded for the whole duration of the study and data analysis.

Sample size and inclusion criteria

Our inclusion criteria depended on our biomechanical and behavioral injury parameters (displacement: 550-750 μm; BMS score $\leq$ 0.5 averaged across both hindlimbs at 1 day post-injury, dpi). According to these criteria, a total of 19 and 18 mice were used in study 1 for the ABT-263-treated and Vehicle-treated experimental groups, respectively. In study 2, each experimental group (Sham, Vehicle and ABT-263) was composed of 9 mice.

Selection of endpoints

The selection of endpoints was based on previous studies and pilot experiments in which we characterized both models. We took in account the different phases of the injury progression (subacute and chronic) in a mouse contusion model and the whole regeneration period (60 dpi) of the zebrafish.

METHOD DETAILS

Spinal cord injury (SCI) and post-operative care

Zebrafish

Animals were anaesthetized in 0.016% tricaine (Sigma, MS222), and a spinal cord crush injury was performed according to a previously described method (Fang et al., 2012). Upon cessation of opercular respiratory movements, the fish were transferred into a fixed thin filter paper (3 cm x 2 cm) placed on crushed ice and positioned on their side with their head pointing left, under a

stereoscope. With a dissecting knife, 4-5 squamae were removed and an incision was made at a distance 4 mm caudal to the brainstem/spinal cord junction. The skin and muscle were cut with a spring scissor until the spinal cord was exposed. The spinal cord was then crushed using Dumont #55 forceps (Fine Science Tools, 11255-20). Special attention was given not to damage the ventral vertebrae under the spinal cord, which may compromise the recovery process. Finally, the wound was sealed with tissue adhesive surgical glue (3M Vetbond™, 1469SB). Zebrafish were allowed to recover at 28°C in individual tanks until different experimental time-points (3, 7, 15, 30 and 60 dpi), upon which they were sacrificed and the spinal cords (5-6 mm width) dissected. In control fish, a Sham injury was performed by making an incision at the side of the animal but leaving the spinal cord intact before sealing the wound.

Mice

Before being assigned to SCI, mice went through a two weeks-period of handling and acclimatization, during which body weight was assessed to ensure ideal surgical weight (18-20 g). Animals were anesthetized using a cocktail of ketamine (120 mg/kg) and xylazine (16 mg/kg) administered by intraperitoneal injection (IPi). For spinal contusion injuries, a laminectomy of the ninth thoracic vertebra (T9), identified based on anatomical landmarks, was first performed (Harrison et al., 2013) followed by a moderate-to-severe (force: 75 Kdyne; displacement: 550-750 μm) contusion using the Infinite Horizon Impactor (Precision Systems and Instrumentation, LLC.) (Scheff et al., 2003). The mean applied force and tissue displacement for each experimental group are shown in Figure S6. There were no differences in injury parameters between experimental groups. After SCI, the muscle and skin were closed with 4.0 polyglycolic absorbable sutures (Safil, G1048213). In control uninjured mice (Sham), the wound was closed and sutured after the T9 laminectomy and the spinal cord was not touched. Animals were injected with saline (0.5 ml) subcutaneously, then placed into warmed cages (35°C) until they recovered from anesthesia and for the following recovery period (3 days). To prevent dehydration mice were supplemented daily with saline (0.5 ml, subcutaneously) for the first 5 dpi. Bladders were manually voided twice daily for the duration of experiments. Body weight was monitored weekly.

Drug treatment

ABT-263 (Selleckchem, S1001, 50 mg/kg/day) or Vehicle (Corn oil, Sigma, C8267) were administered by oral gavage, as described previously (Chang et al., 2016). In our experimental model, oral gavages were performed for 10 consecutive days starting at 5 dpi until 14 dpi. Animals were mildly sedated with isoflurane to facilitate handling and gavage procedure, which was conducted using disposable flexing feeding needles (Cadence Science, #9928B). After SCI, mice were randomly assigned to each treatment cohort for each endpoint group. The impact of targeting SCs with ABT-263 was evaluated in two separate studies. In study 1, which comprised the functional analysis at the behavioral and cellular level, animals were distributed between 3 endpoint groups: 15 dpi (n = 10), 30 dpi (n = 14) and 60 dpi (n = 13). Study 2 aimed at assessing the secretory profile using a cytokine array as well as the protein/mRNA expression of senescence markers (namely p16/*cdkn2a*) after ABT-263 treatment. This study was composed of a single endpoint group: 15 dpi (n = 18).

Dasatinib (Sigma, SML2589, 5 mg/kg/day) + Quercetin (Sigma, 1592409, 50 mg/kg/day) or Vehicle (10% PEG400, Sigma, 81172) were administered by oral gavage, as described previously (Zhu et al., 2015). In our experimental model, oral gavages were performed for 10 consecutive days starting at 5 dpi until 14 dpi. Animals were mildly sedated with isoflurane to facilitate handling and gavage procedure, which was conducted using disposable flexing feeding needles (Cadence Science, #9928B). After SCI, mice were randomly assigned to each treatment cohort for each endpoint group, 15 dpi (n = 7) and 30 dpi (n = 15).

Within the same cage animals received different treatments to exclude specific environmental cage input. Experimenters were blinded for the whole duration of the study by coding the treatment.

Behavior assessment

Basso mouse scale (BMS)

Two weeks before the beginning of the study mice were habituated to the open-field arena to decrease anxiety and distress. On the day of the behavioral test two investigators, blind to treatment, assessed mouse hind limb function and locomotion using the BMS (Basso et al., 2006). Locomotor behavior (BMS scores and subscores) was assessed at 0 (baseline), 1, 3, 5, 7, 10, 12, 15, 21, 30, 45 and 60 dpi.

Horizontal ladder (HL)

On the previous week before SCI, mice were trained to walk along a HL as previously described (Cummings et al., 2007). This task requires mice to walk across a HL that consists of a 60 cm length x 8 cm width transparent corridor with rungs spaced 1 cm apart. A mirror was placed underneath the ladder and mice were video-recorded from the side view to be able to see paw placement on the rung in the mirror. Home cage bedding and/or treat-pellets were placed at the end to stimulate motivation. Ideally, each mouse was able to perform at least three successful trials along the ladder. The three best attempts were scored. A paw falling below the rungs of the ladder during a step in the forward direction was counted as one mistake. The total number of mistakes was averaged across the three trials per mouse and quantified as mistakes per centimeter. The total number of positive and negative events for each rung in each attempt were also quantified and are divided as singular positive events (plantar step, toe step and skip) or singular negative events (slip, miss and drag). Baseline data were assessed 1 day before SCI. Mice were tested on the HL at 15, 30 and 60 dpi.

Incremental thermal plate (ITP)

Each mouse was placed into the observation chamber of the IITC's Incremental Hot Cold Plate (IITC Inc. Life Science) with a starting temperature of 37°C, as previously described (Yalcin et al., 2009). The plate was then either heated up to 49°C or cooled down to 0°C

at a rate of 6°C per minute until the animal showed nocifensive behavior involving either hindpaw. The typical response was hindpaw licking, shaking and lifting of the paw, jumping and extensor spasm. The plate temperature evoking any of these nocifensive reactions confined to any hindpaw was regarded as the noxious heat/cold threshold of the animal. Following the recording of the threshold temperature, the animal was immediately removed from the plate. The threshold measurement was repeated after 30 minutes and the mean of the two thresholds was considered as the control noxious heat/cold threshold of the animal. Animals were tested in the ITP at 30 and 60 dpi.

Bladder function

Bladder function was grossly evaluated by attributing an averaged bladder score (from 0 to 3) to the two daily urine collections, depending on the amount of retained urine (0 – empty bladder; 1 – small bladder; 2 – medium bladder; 3 – large/full bladder). Bladder voiding times, as well as voiding-responsible experimenters, were maintained consistent throughout the experiment.

Tissue processing

Zebrafish

The vertebral column of adult zebrafish was dissected and fixed in 4% paraformaldehyde (PFA) at 4°C overnight. After fixation, the spinal cord was isolated from the vertebral column. Samples were washed 3 times in phosphate-buffered saline (PBS) during the day and incubated overnight with SA-β-gal staining solution (see details below). Following the SA-β-gal staining protocol, samples were cryoprotected in 30% sucrose/0.12 M phosphate buffer (PB) for a minimum of 72 hours at 4°C or until the tissue sinks to the bottom of the vial, followed by another embedding in 7.5% gelatin (Sigma, G6144)/15% sucrose/0.12 M PB and subsequently frozen. The samples were cryosectioned in 12 μm-thick longitudinal slices using a Cryostat Leica CM 3050S and either processed for immunohistochemistry or counterstained with eosin for SA-β-gal quantifications.

Mice

Mice were anesthetized with ketamine/xylazine mix (120 mg/kg + 16 mg/kg, IPi) and then transcardially perfused with 0.9% sodium chloride followed by 4% PFA. Post-mortem anatomical assessment of the T9 was confirmed to ensure correct thoracic contusion. Spinal cords were removed, post-fixed in 4% PFA for 2 hours and then incubated overnight with SA-β-gal staining solution (see details below). Samples (1 cm in length) were then submitted to the same cryoprotection/embedding and cryosection/staining procedures as for zebrafish spinal cords. Tissue sections were cut in series either transversally (10 μm thick, 10 slides per series) or longitudinally (10 μm thick, 6 slides per series). For each time-point, samples were distributed as equally as possible in cuts along the coronal (rostral-caudal) axis and horizontal (dorsal-ventral) axis. Slides were stored at −20°C until needed. Every block, as well as every slide, was coded until the end of each analysis.

SA-β-gal staining

SA-β-gal activity was determined in isolated spinal cords using the SA-β-gal kit (Cell Signaling, #9860) according to manufacturer's instructions, with minor adaptations. Spinal cords were fixed overnight in 4% PFA, washed three times in PBS and stained overnight at 37°C using the SA-β-gal staining solution (pH 5.9-6.1, prepared according to kit's instructions). The samples were then washed in PBS, fixed in 4% PFA for 4 hours, washed 3 × 5 minutes in PBS and embedded in sucrose as described above.

Immunohistochemistry

To perform immunostaining in sections, the gelatin was removed from the cryosections using PBS heated to 37°C (4 × 5-minute washes). After incubation with blocking solution for 2 hours at room temperature, the sections were incubated overnight with primary antibody solution at 4°C. Sections were then washed in PBS/0.1% Triton X-100 and incubated with the secondary antibody (1:500) and 1 mg/ml DAPI (Sigma, D9564) for 2 hours at room temperature. Details on the blocking solutions, primary and secondary antibodies used are described in Table S1 and Key resources table. After incubation with the secondary antibodies, the sections were washed in PBS and mounted in Mowiol mounting medium.

For 5-Bromo-2′-deoxyuridine (BrdU) incorporation, the day before collection of the spinal cord, zebrafish were injected intraperitoneally with 50 μL of 2.5 mg/ml BrdU solution (in 110 mM NaCl pH 7.2) using an insulin syringe. To detect BrdU in cryosections, prior to the antibody staining procedure, the DNA was denatured for 30 minutes at 37°C in pre-heated 2 N HCl followed by three 5-minute washes in 0.1 M Tris pH 8.5 and two washes in PBS.

Imaging

The colorimetric images of SA-β-gal-stained sections were acquired using a NanoZoomer-SQ digital slide scanner (Hamamatsu) or a Leica DM2500 brightfield microscope with HC PL FLUOTAR 20x / 0.5 NA Dry objective. Immunostained sections were imaged using a motorized Zeiss Axio Observer widefield fluorescence microscope equipped with an Axiocam 506 mono CCD camera or a Zeiss Cell Observer SD confocal microscope equipped with an Evolve 512 EMCCD camera (Plan-Apochromat 20x / 0.80 NA Dry objectives). Each image is a maximum intensity projection of a z stack acquired from the 10/12 μm cryosection. F4/80- and GAP43-stained immunosections were imaged using a Zeiss Axio Scan.Z1. The processing of acquired images was performed using Zeiss ZEN 2 (blue edition) and the image analysis software Fiji. Adobe Illustrator was used for assembly of figures.

Quantification of SA-β-gal$^+$ cells

To characterize the senescence profile in both models, SA-β-gal$^+$ cells were manually quantified (using a Cell Counter plugin in Fiji) and averaged across 4 (zebrafish) or 8 (mouse) longitudinal sections spanning the ventral horn and imaged at the lesion periphery (from 0.5 to 2.5 mm laterally to the lesion) at 3, 7, 15, 30 and 60 dpi. In Sham-injured animals, sections were imaged laterally to the injury segment.

Senolytic effects after SCI were evaluated by manually quantifying and averaging the number of SA-β-gal$^+$ cells in 10 transversal sections at the lesion periphery (from 0.5 to 2.5 mm rostrally or caudally to the lesion) at 15, 30 and 60 dpi. Two distinct quantifications were performed: one in the total sectional gray matter and other only in the ventral horn.

SA-β-gal$^+$ cells were quantified in the gray matter but not in the white matter and normalized to the total area covered (cells/mm^2).

White matter sparing

One set of sections spaced 0.1 mm apart and spanning the entire block was stained with FluoroMyelin^{TM} Green (ThermoFisher Scientific, F34651) for 1 hour. The percentage of cross-sectional area (% CSA) with spared myelin was calculated by manually measuring the area of stained myelin in Fiji and normalizing it to the total cross-sectional area in each section (every 0.1 mm) along 2 mm rostrally and caudally from the lesion epicenter, which was identified as the section with the smallest % CSA.

Axonal preservation

GAP43$^+$ axons were quantified at specific distances from the lesion epicenter, as previously described (Almutiri et al., 2018; Hata et al., 2006). At 30 and 60 dpi, GAP43$^+$ fibers were counted in the white matter of the ventral horn region using a custom-made macro in Fiji that, after manually establishing a threshold value and defining the lesion epicenter, determined the number of positive fibers every 1 mm from 4 mm rostral (above) to 4 mm caudal (below) from the lesion epicenter and normalized it to the tissue length covered in each measurement. Quantifications were averaged across 3 longitudinal spinal sections per biological sample and axon count was calculated as number of GAP43$^+$ fibers per millimeter (fibers/mm).

Fibrotic scar area and length

A distinct set of sections was stained with anti-PDGFRβ and anti-GFAP in order to identify the fibrotic scar area and border. The percentage of fibrotic scar area at lesion epicenter was calculated by manually outlining the PDGFRβ$^+$ area and normalizing it to the total cross-sectional area. Measurements were performed using Fiji tools. Using the same set of sections, the rostral and caudal extents of PDGFRβ$^+$ fibrosis were determined for each lesion, and total lesion length was calculated by multiplying the number of sections containing fibrotic tissue by the distance between each section (0.1 mm).

Inflammation

Spinal sections 0.1 mm apart extending from 1 mm rostral to 1 mm caudal to the lesion epicenter were stained for the pan macrophage marker F4/80. Macrophages form a network within the central lesion core and are difficult to be individually distinguished, (Brennan and Popovich, 2018). Therefore, the measurements of F4/80$^+$ cells were expressed as a percentage of the total cross-sectional area. In each section. the area of F4/80$^+$ staining was measured using a custom-made macro in Fiji that, after manually setting a threshold value, calculated the F4/80$^+$ area and normalized it to the total cross-sectional area. Quantifications were performed at the lesion epicenter, 0.6 mm above (rostral) the epicenter and 0.6 mm below (caudal) the epicenter.

Quantitative real-time PCR

Total RNA was extracted from zebrafish and mouse spinal cord samples (1 cm of tissue spanning the lesion site) using TRIzol (Invitrogen)/ chloroform and purified using the RNA Clean & Concentrator-5 kit (Zymo Research), according to manufacturer's instructions. RNA concentration was determined by NanoDrop (Thermo Scientific). cDNA synthesis was performed using the iScript Reverse Transcription Supermix for RT-qPCR (Bio-Rad), according to manufacturer's instructions. qPCR was performed using 7500 Fast Real-Time PCR System (Applied Biosystems) and Power SYBR Green PCR Master Mix (Applied Biosystems). For each cDNA sample, three technical replicates were included. Relative mRNA expression was normalized to glyceraldehyde-3-phosphate dehydrogenase (GAPDH) (zebrafish) or cypA (mouse) mRNA expression using the ΔΔCt method. Primers used for qPCR are listed in Table S2.

Western blot

Protein samples were prepared by homogenizing mouse spinal cord samples (1 cm of tissue spanning the lesion site) in lysis buffer (PBS + 1% Triton X-100) containing protease and phosphatase inhibitors. Protein concentrations were determined by BCA Protein Assay (Pierce). For western blot analysis, 50 μg of protein content of each sample was loaded and separated by SDS-PAGE gel (4–15%; Bio-Rad). After the transfer, the blots were incubated overnight at 4°C with a polyclonal antibody against p16 (1:1000, rabbit; ProteIntech), followed by incubation with HRP-conjugated secondary antibody. GAPDH monoclonal antibody (1:1000, mouse; ThermoFisher Scientific/AM4300; RRID: AB_2536381) was used as loading control. Blots were developed in ECL solution and exposed onto Amersham 680 (GE Healthcare) for 5 minutes. The intensity of the specific bands was quantified using Image Studio Lite software.

Cytokine array

Cytokine and chemokine expression was measured using the Proteome Profiler Mouse XL Cytokine Array (ARY028; R&D Systems, Minneapolis, MN, USA) in spinal cord homogenates, prepared in the same manner as for western blot analysis, and used according to the manufacturer's instructions. In brief, nitrocellulose membranes were blocked for 1 hour; then, spinal cord homogenates containing 200 μg of protein content was added and incubated overnight at 4°C. The following day, the membranes were washed and a detection antibody cocktail (R&D Systems) was added. The membranes were incubated with the detection antibody for 1 hour, washed and incubated with streptavidin-HRP for 30 minutes. Membranes were washed and spots detection was visualized by addition of enhanced chemiluminescence reagent. The membranes were imaged on an Amersham 680 (GE Healthcare) and dots density was quantified using Image Studio Lite software.

QUANTIFICATION AND STATISTICAL ANALYSIS

GraphPad Prism 7 was used for data visualization and SigmaPlot 14 for statistical analysis. The senescence profile after SCI was analyzed using a one-way ANOVA followed by a Bonferroni's post hoc test (zebrafish) or a non-parametric Kruskal-Wallis one-way ANOVA test (mouse). BMS and Bladder Score data were analyzed using a two-way repeated-measures ANOVA, followed by a Bonferroni's post hoc test. HL, ITP, white matter sparing, axonal preservation, fibrotic area and inflammation data were analyzed using a normal two-way ANOVA, followed by a Bonferroni's post hoc test. qPCR data were analyzed using an unpaired t test, while data from western blotting and the cytokine array were analyzed using a one-way ANOVA followed by a Bonferroni's post hoc test. All data were expressed as mean ± SEM, with statistical significance determined at $p\text{-value}s < 0.05$. Details on statistical parameters, including sample numbers and precision measures (e.g., mean and *p-value*s) are described in the figure legends or in the main text.